Received: 15 December 2022 | Revised: 29 October 2023 | Accepted: 8 November 2023

DOI: 10.1002/dep2.261

The Depositional Record Open Access
A journal of the International Association of Sedimentologists
WILEY

ORIGINAL RESEARCH ARTICLE

Application of micro-CT to resolve textural properties and assess primary sedimentary structures of deep-marine sandstones

P. H. Cornard[1] | **G. Degenhart**[2,†] | **P. Tropper**[3] | **J. Moernaut**[1] | **M. Strasser**[1]

[1]Institute of Geology, University of Innsbruck, Innsbruck, Austria

[2]Department of Radiology, Core Facility Micro CT, Medical University of Innsbruck, Innsbruck, Austria

[3]Institute of Mineralogy and Petrography, University of Innsbruck, Innsbruck, Austria

Correspondence
P. H. Cornard, Department of Geology, University of Innsbruck, Innrain 52, Innsbruck, Austria.
Email: pauline.cornard@uibk.ac.at

Funding information
Austrian Science Fund, Grant/Award Number: Flow-Dynamic-Fan project/M3065N

Abstract

Over the past decade, there has been growing interest in the sedimentological community to use micro X-ray computed tomography to analyse microfacies in sediment cores. However, little attention has been paid to the application of micro-computed tomography in lithified deposits, even though this can allow their texture to be characterised in three dimensions, providing key information about sedimentary structures. A novel application of micro-computed tomography in lithified sediment-gravity flow deposits is presented with the objective of characterising their internal 3D sedimentary structures. This technique is applied to three deep-marine sandstones showing different compositional properties: Cretaceous Gosau Group (Austria), Eocene Hecho Group (Spain) and the Oligocene Annot Formation (France). From micro-computed tomography data the size of particles and their distribution throughout the sample is reconstructed in 3D permitting a better visualisation of sedimentary textures. Particle distributions computed from micro-computed tomography are similar to those computed from thin section image analysis, corroborating the reliability of the micro-computed tomography to evaluate grain-size trends. Micro-computed tomography is complemented with micro-X-ray fluorescence and thin section petrographic analyses. In cases where mineral composition or grain size are homogeneous or matrix and grains have similar mineral composition, sedimentary structures do not appear visible from micro-X-ray fluorescence or thin section analyses. By separating particles based on their computed tomography density, it is possible to isolate the coarsest fraction, highlighting the sedimentary structures. This study demonstrates (i) the potential of micro-computed tomography in analyses of sedimentary structures from outcrop data and (ii) the importance of the mineralogical composition and degree of grain sorting in assessing the origin of structureless deposits. Considering the importance of visualising sedimentary structures when interpreting depositional processes, micro-computed

[†]Equally contributing first author.

tomography is a new and reliable tool to assess the physical properties of sandstones and to analyse their internal 3D sedimentary structures.

KEYWORDS
micro-CT, sandstones, sedimentary structures, turbidites

1 | INTRODUCTION

Over the past several decades, medical X-ray computed tomography (CT) has been widely used in the Earth Sciences for imaging geological samples (Ketcham & Carlson, 2001). It has gained acceptance as a routine core analysis tool highlighting surface as well as internal features, including bedding, sedimentary structures, fractures or cement distribution (Orsi et al., 1994; Baraka-Lokmane et al., 2009; Nelson et al., 2009; Penkrot et al., 2018). Although medical CT scanners have significantly improved in terms of image quality and imaging speed, the spatial resolution remains limited due to the size of the sample and the diameter of the gantry (e.g., fitting a human body). Over the last decade a new research domain, termed micro-CT, has developed in high-resolution X-ray tomography (Cnudde & Boone, 2013). Although micro-CT can only be applied to small samples (geological samples varying from 1 mm to 10 cm), the resolution is much higher than medical-CT, down to 2.5 µm. Since then, micro-CT techniques have been widely applied in Earth Sciences, especially in (i) 3D pore characterisation (McCoy et al., 2006; Polacci et al., 2010) for reservoir characterisation (Coenen et al., 2004; Sok et al., 2010; Tiwari et al., 2013; Kim et al., 2016; Schmitt et al., 2016; Lei et al., 2019; Su et al., 2022) and soil analysis (Sleutel et al., 2008; Munkholm et al., 2012; Singh et al., 2021); (ii) 3D grain analysis (Carlson, 2006; Jerram et al., 2009; Cnudde et al., 2011) particularly for minerals with metallurgical significance (Kyle & Ketcham, 2015; Ghorbani et al., 2011; Evans et al., 2015); (iii) structural processes (Otani et al., 2010; Siddiqui et al., 2010; Wildenschild & Sheppard, 2013), especially in fracture analysis (Bertels et al., 2001; Kumari et al., 2018; Yang et al., 2020). The clastic sedimentology community also shows a growing interest in using micro-CT, particularly to highlight microfacies in sediment cores (Bendle et al., 2015; Van Daele et al., 2016; Wils et al., 2021; Sabatier et al., 2022; Vermassen et al., 2023). Despite this increased attention, few studies have tested the potential of micro-CT to analyse internal primary sedimentary structures in lithified rocks.

Primary sedimentary structures in sediment-gravity flow (SGF) deposits are produced by physical processes during sediment transport and deposition (Middleton, 1965; Allen, 1970; Hiscott & Middleton, 1980; Arnott & Hand, 1989; Komar, 1989; Baas, 2004; Sumner et al., 2008; Talling, 2013) and are key to interpreting parts of the ancient sedimentary record. In the depositional record, primary sedimentary structures are rendered visible by variations in grain size (e.g., grading, sorting) and/or mineral composition (e.g., higher concentration of clay, micas or organic matter) within the lamination set (Kuenen, 1966; Campbell, 1967; Paola et al., 1989; Cheel, 1990; Best & Bridge, 1992). Although internal sedimentary structures of lithified SGF deposits are well recognised in the rock record (Kiminami & Kontani, 1979; Stow & Piper, 1984; Stevenson et al., 2020) and reproduced in flume-tank experiments (Arnott & Hand, 1989; Leclair & Arnott, 2005; Sumner et al., 2008; Cartigny et al., 2013) and by numerical modelling (Jiang, 1995; Legros, 2002), there is a lack of characterisation of these structures in three dimensions (3D) and at the micro-scale.

This study aims to discuss the potential of micro-CT to characterise the texture of lithified SGF deposits to better assess their internal primary sedimentary structures. It is also important to take into account the mineral composition and the post-depositional processes (i.e., diagenesis) into the visualisation of sedimentary structures. However micro-CT is unable to determine mineral phases, and therefore is complemented with micro X-ray fluorescence (micro-XRF) and thin section petrographic analyses. To better assess textural characteristics at the origin of sedimentary structures, particle size is directly computed from micro-CT data. This multi-technique approach is applied on SGF deposits with contrasting mineral composition cropping out in ancient deep-marine strata: Upper Cretaceous Gosau Group (Austria), Middle Eocene Hecho Group (Spain) and the Upper Eocene-Lower Oligocene Annot Formation (France). The objective of this paper is to show that the micro-CT technique (and related computed particle size) in conjunction with chemical analyses provide an innovative and accurate method to analyse primary sedimentary structures in 3D in lithified SGF deposits.

2 | METHODS

2.1 | Fieldwork

Samples were collected in three study areas with varying mineral composition: the Upper Cretaceous Gosau Group (Austria) that is rich in dolomite, the Middle Eocene Hecho Group (Spain) with a high calcite content, and the Oligocene Annot Formation with a low carbonate content. Samples were collected from turbidites with different kinds of internal sedimentary structures.

The Upper-Cretaceous Gosau Group is a synorogenic, siliciclastic sedimentary system that was deposited in the Muttekopf Basin (Western Austria) and crops out in the Northern Calcareous Alps of the Eastern European Alps (Figure 1A). The Gosau Group in the Muttekopf Basin occurs in a syncline in the hanging wall of the Inntal Nappe, composed of the Hauptdolomite Triassic carbonate shelf (Wagreich & Faupl, 1994). The Gosau sample was collected from Megasequence 2 (Ortner, 2001; Figure 1B).

The Hecho Group is an *ca* 4 km succession of Middle Eocene deep-marine siliciclastic sediments infilling the South Pyrenean foreland Ainsa and Jaca basins (Mutti et al., 1977) (Figure 1C). The sample (referred to as the Hecho sample in this study) was collected from the Ainsa Basin, and more precisely from the Ainsa System cropping out in the Ainsa Quarry (Figure 1D).

The Tertiary Grès d'Annot Formation of south-east France is a Late Eocene-Early Oligocene sand-rich deep-marine system deposited in a wedge-top basin as part of a foreland system developed in front of the Alpine Orogen (Pickering & Hilton, 1998). The Grès d'Annot Formation is preserved in isolated areas termed "sub-basins". The Annot sample was collected from the Annot sub-basin (Figure 1E,F).

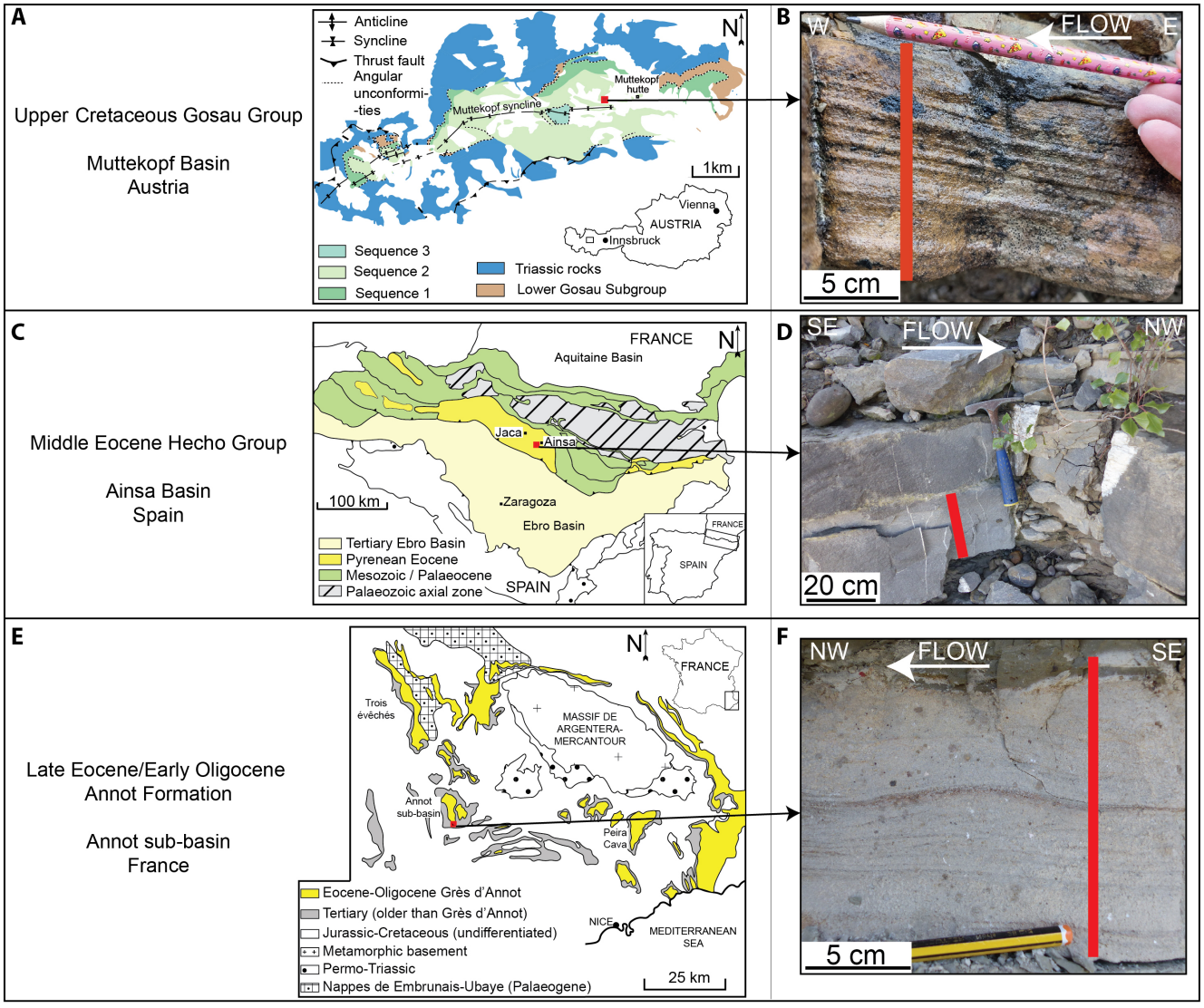

FIGURE 1 (A) Simplified geological map of the Upper Cretaceous Gosau Group in the Muttekopf Basin (modified from Ortner et al., 2016). Red square indicates the sample location. (B) Turbidite from the Upper-Cretaceous Gosau Group in which sample was taken. Geographical coordinates: N47.264204°, E10.663339°. Red line indicates the coring location. (C) Simplified geological map of the South Pyrenean foreland basin, including the Ainsa and Jaca basins filled with the deposits of the Middle Eocene Hecho Group (modified from Vergès et al., 2002). Red square indicates the sample location. (D) Turbidite from the Hecho Group (Ainsa Quarry) in which sample was taken. Geographical coordinates: N42.403912°, E0.148392°. Red line indicates the coring location. (E) Simplified geological map of the Grès d'Annot Formation of South-East France (modified from Pickering & Hilton, 1998). Red square indicates the sample location. (F) Turbidite from the Grès d'Annot Formation (Annot sub-basin) in which sample was taken. Geographical coordinates: N43.960498°, E6.681391°. Red line indicates the coring location.

Palaeoflow was interpreted in the field based on flute casts or the orientation of ripple cross-lamination.

2.2 | Sample preparation and workflow

Samples collected in the field (Figure 2—step 1) were drilled with a 12 mm diameter drill bit (Figure 2—step 2). The coring technique was chosen as rounded samples are more suitable for micro-CT analyses compared to samples with sharp edges that produce significant artefacts. In the micro-CT scanner, samples were consistently oriented in the plane parallel to the palaeoflow direction. Micro-CT data are used (i) to evaluate the internal 3D structures of the samples based on the CT density contrast between the different minerals and, (ii) to compute the size and distribution of particles in 3D.

Once micro-CT data were collected, core samples were cut in half and analysed by micro-XRF on the plane surface (Figure 2—step 3). Because grains are usually oriented in specific directions with respect to the palaeoflow (Hiscott & Middleton, 1980; Arnott & Hand, 1989), samples were cut parallel to the palaeoflow direction in order to capture as much information as possible about flow characteristics. Cut surfaces were gently polished with 120 grit sand-paper to increase the quality of micro-XRF maps. However, the amount of polishing was limited to minimise disruption of the primary grain fabric, and therefore misalign the micro-CT data with micro-XRF maps and images of thin sections. Micro-XRF analysis provides the chemical element distribution on the sample surface (see Section 2.5). To properly align (register) the micro-XRF plane with the micro-CT scan, a second scan was performed on the half-core samples. The second scan was aligned with the original scanned volume resulting in a transformation matrix that now orients the original volume with the cutting plane of the micro-XRF and thin section. After aligning the micro-CT and micro-XRF images and by combining chemical elements together in the micro-XRF maps, it is possible to assign the observed densities in the micro-CT to specific minerals and determine their distribution throughout the sample and within sedimentary structures (see Section 2.4.1 for more details).

Thin sections were cut on the surface plane of the half core to compare micro-XRF data with mineral data from thin sections (Figure 2—step 4). High-resolution photomicrographs were then analysed to determine the size and distribution of grains (see Section 2.7).

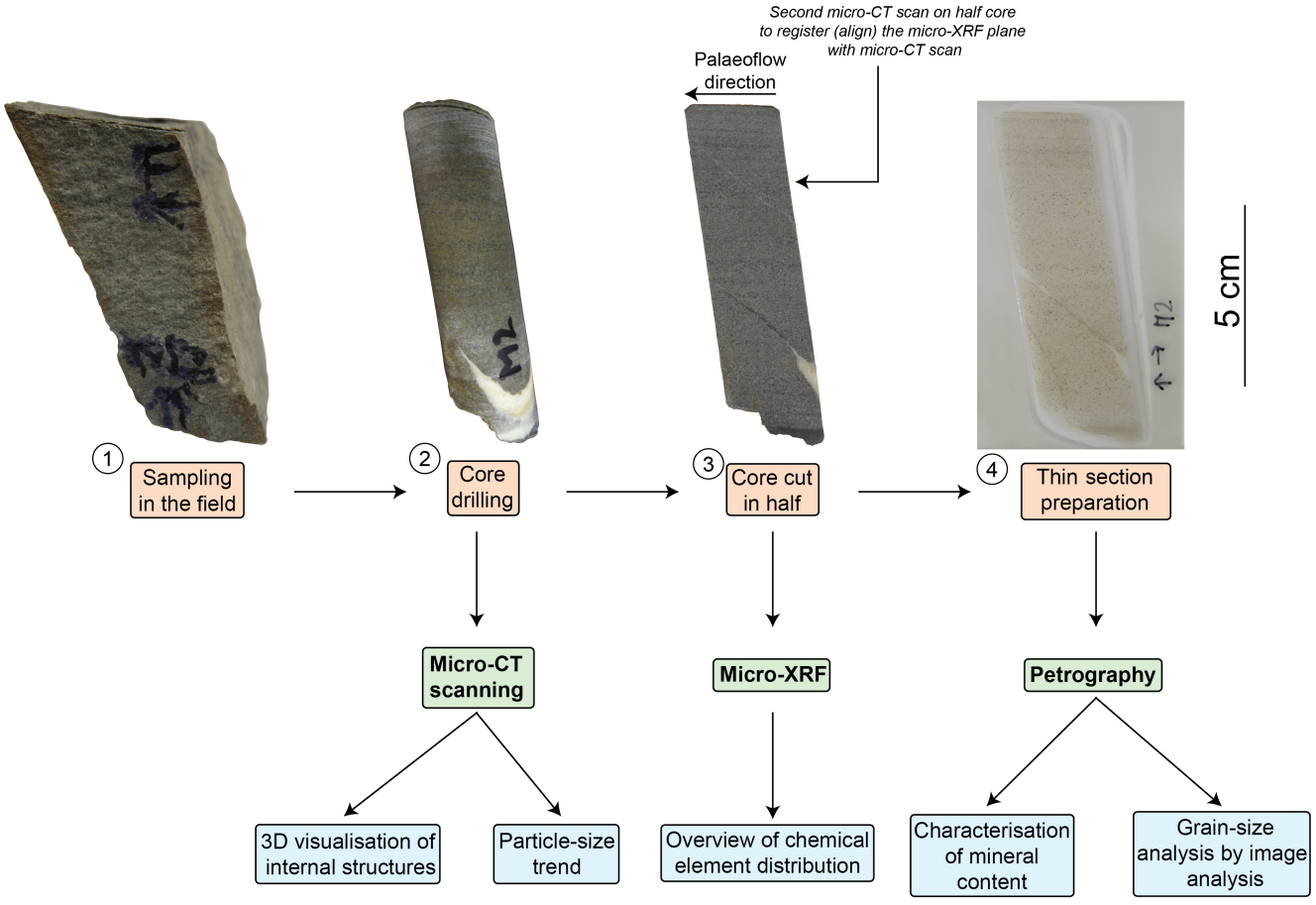

FIGURE 2 Workflow of the methodology used in this study.

2.3 | Micro-CT acquisition

Micro CT imaging was performed using a vivaCT 40 (Scanco Medical AG, Brüthisellen CH) at the Medical University of Innsbruck. The vivaCT 40 is based on the cone beam geometry developed by Feldkamp et al. (1989). Being a quantitative CT, the vivaCT 40 does not represent image greyscales using the Hounsfield unit scale (HU) as medical CT does, but uses the density of hydroxyapatite $Ca_{10}(PO_4)_6$ $(OH)_2$, referred to as HA in this study, resulting in greyscales following a scale of mgHA/cm^3. This scale was introduced in bone quality assessments to directly interpret the mineral content of a bone volume. An advantage of using such a scale is that in comparison to HU the scale has no negative values. Calibration phantom provided by the manufacturer and containing five defined volumes of increasing mineral density is used to achieve HA scaling. Calibration phantom is routinely used to check calibration. The scanning parameters were set to optimise resolution and image quality (signal to noise ratio (SNR) and minimise image artefacts). Scanner settings were a voltage of 70 kV, a 114 µA current, an integration time (time of X-ray exposure per projection) of 600 ms, a field of view (FOV) of 21.5 mm and a hardware binning of 2. These settings create a 1024 × 1024 image matrix with an iso voxel size of 21 µm. Assuming the general rule that a minimum 3-pixel diameter is needed to distinguish a single object, the minimum resolvable object size is *ca* 63 µm. Therefore, grains smaller than very-fine sand are not resolvable. For reconstruction, the automated process provided by the manufacturer was minimally adapted (ring artefact suppression set to maximum).

2.4 | Image processing of micro-CT

Image post-processing and visualisation were performed using the Scanco Medical software suite for micro-CTs in combination with Image Processing Language (IPL; Institute for Biomedical Engineering ETHZ, University of Zürich; Rüegsegger, et al., 1996). For evaluating particle size, a standardised procedure was developed, including multiple thresholding (segmentation), textural evaluation and textural resolution along the Z-axis (Figure 3; Sections 2.4.1 to 2.4.3). Due to the batch operational structure of IPL, all the steps for image processing, except the threshold selection, are fully automated on the Scanco Medical Platform. Computation time varies depending on

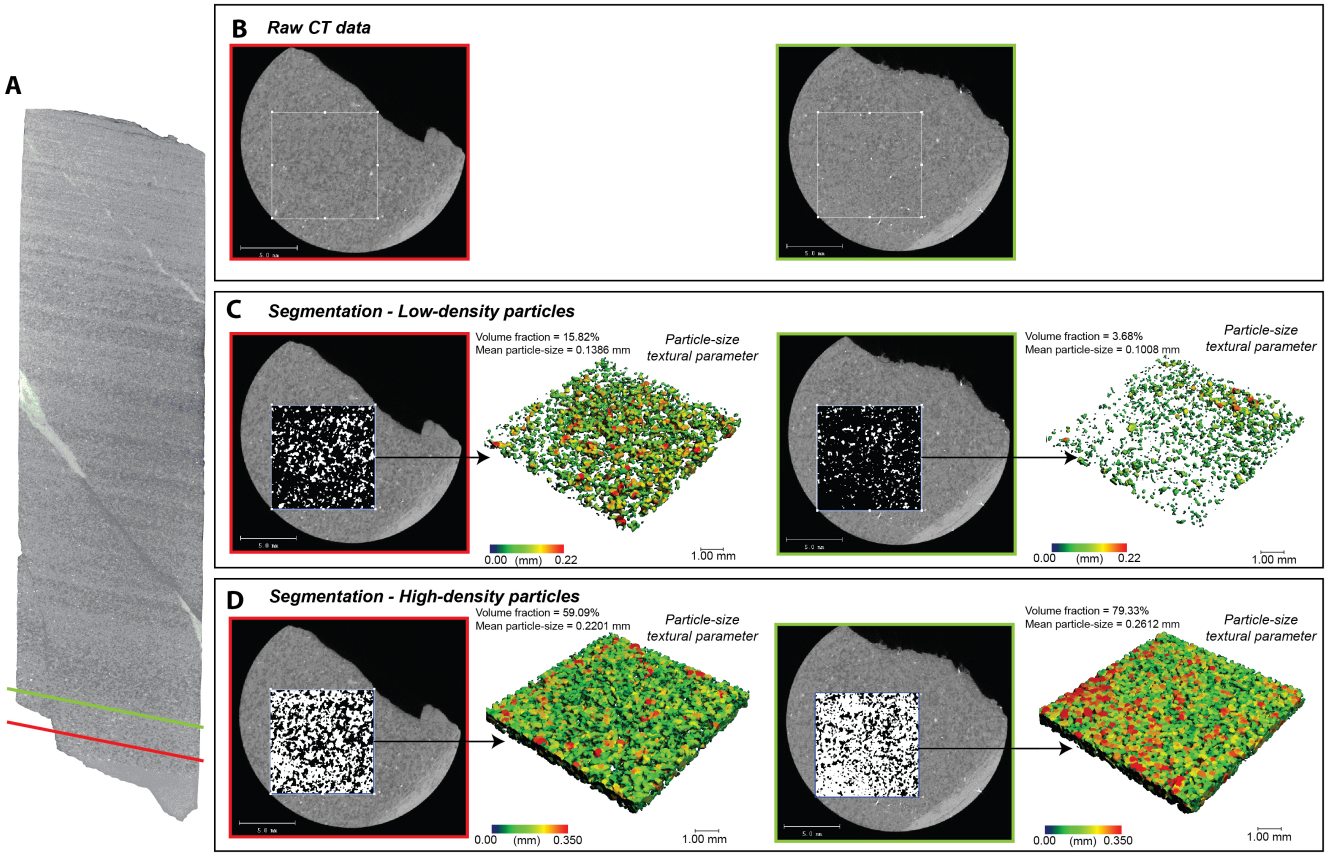

FIGURE 3 (A) Micro-CT native image with two layers marked in green and red. (B) Axial view of the red and green layers marked in (A) with the defined contour for the evaluation; additionally, noise reduction was applied. (C, D) Segmentation and false colour codes imaging of (C) low-density particle distribution and (D) high-density particle distribution in the two layers.

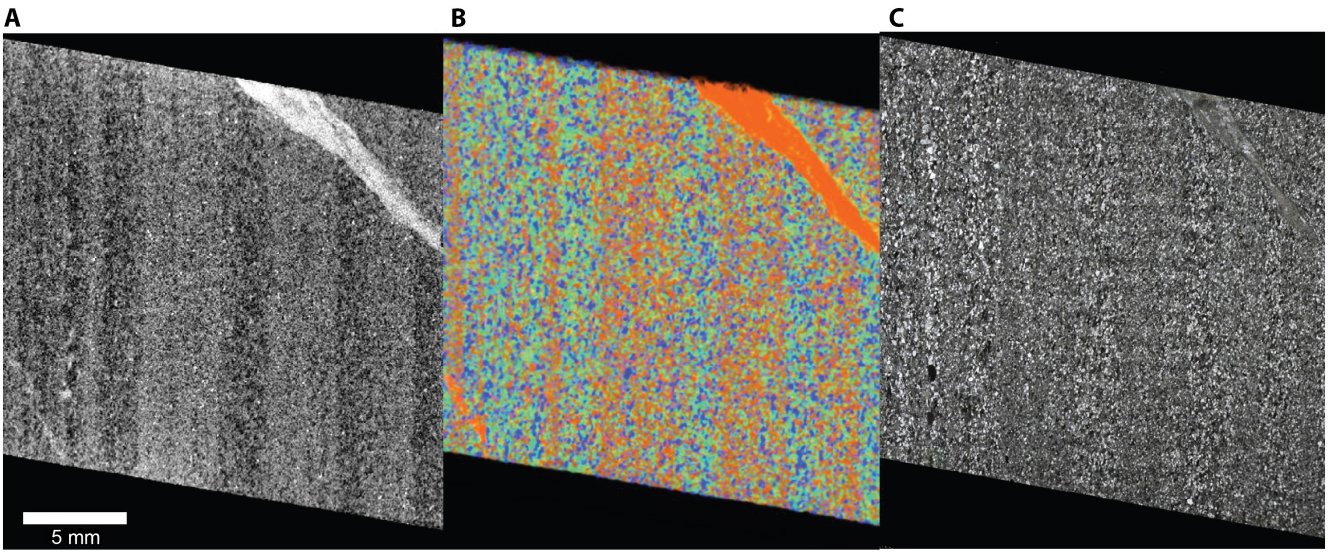

FIGURE 4 Comparison between micro-CT, micro-XRF and thin section images from the Gosau sample. (A) Micro-CT image with optimised image contrast (dark colours: low-density particles; light colours: high-density particle). (B) Micro-XRF image (Green: Silica; Blue: Aluminum; Orange: Calcium). (C) Thin section image.

the analysed volume of the sample (e.g., two days for the Gosau sample).

For a proper volumetric evaluation of the whole sample, pore space with the same density as the surrounding medium (air) has to be taken into consideration for defining the outer contour of the sample. For example, pore structures could be connected to the surface of the object and channels (e.g., interconnected pores) could propagate through the sample and alter the calculation of the total volume of the sample. A new contouring algorithm was developed including pores and solids into a single outer contour (see Supplemental Material S1 for details). For this study, the new contouring algorithm was applied to the Gosau sample but not the larger Annot and Hecho samples due to memory overflow, instead a rectangular volume of interest (VOI) was analysed.

2.4.1 | Image smoothing and threshold estimations

For further smoothing and increasing the SNR, a Gaussian filter is convolved with the image space (settings Gauss:2 Sigma:1.3; Supplemental Material S2).

Guided by Boone et al. (2011) and Bam et al. (2020) that the linear attenuation of X-rays correlates with elemental atomic number and the mass density of the analysed material, assumptions for greyscale domains being correlated to specific mineral compositions must be seen as valid. Combining this assumption with the elemental data from micro-XRF analysis, an estimate of the linear attenuation in CT for identifying minerals is indirectly possible. Aligning the micro-CT images with the micro-XRF data (see Section 2.2), allows the visual differentiation of silicate-dominated from carbonate-dominated lamination (Figure 4).

For the three sandstones in this study, relevant structures have densities between 400 and 2400 mgHA/cm^3. Higher values are not considered as they correlate with high-density minerals (e.g., pyrite). These high-density minerals have the disadvantage of producing artefacts (starburst artefact; Ketcham & Carlson, 2001) around their borders and, therefore, are not accurately distinguished. Based on these observations and the knowledge that these samples are sandstones, three greyscale domains were selected representing low-density, middle-density and high-density particles. These domains were selected as they best describe the chemical and mineral information gained from micro-XRF and thin section analyses, and the greyscale phases seen in the micro-CT images. Based on the mineral information and their related X-ray attenuation, the following starting settings for greyscale domains are suggested: a low threshold window of 400 to 1100 mgHA/cm^3; a middle threshold window of 1100 to 1500 mgHA/cm^3; and a high window of 1500 to 2400 mgHA/cm^3. However, due to the occurrence of partial volume effects (Peyrin et al., 1998), combined with differences in mineral composition (depending on different volume fractions between silicates, carbonates and their respective grain sizes), these suggested threshold windows have to be adapted for each sample. These thresholds are adapted subjectively based on the visible greyscale differences and borders of particles to optimally fit the micro-CT images. For example, for the silicate-rich Annot sample dominated by low CT density, threshold

windows were lowered compared to suggested thresholds. On the other hand, thresholds for the Gosau sample were shifted towards higher CT density due to the presence of the calcite-filled fracture (see Supplemental Material S3).

2.4.2 | Calculation of textural parameters

Each threshold is fed separately into the calculation pipeline where stepwise volumetric density and textural parameters are evaluated (Figure 3). The following parameters are evaluated for each slice of each sample and as a measure for the whole volume:

- Volumetric parameters: total volume, volume of the segmented material, and volume fraction of the segmented material to the whole volume.
- Density parameters: mean density of the material is calculated and represented in mgHA/cm^3
- Particle size: under the assumption that areas with the same density window are composed of the same material, the particle size is calculated using the bubble-growing algorithm of Hildebrand and Rüeggsegger (1997).

2.4.3 | Particle size

Particle size is calculated using the algorithm of Hildebrand and Rüeggsegger (1997), which originally was developed to determine the mean thickness of bone trabecular structures. The algorithm assumes growing virtual bubbles within a segmented volume. Starting from randomly selected voxels within the object, bubbles grow by integrating neighbouring voxels of the same object (Figure 5A). As soon as the bubble encounters two edges, a potential short axis is found and labelled to each voxel belonging to the bubble (Figure 5B). This step is to be repeated until all voxels inside the analysed sample are labelled by at least one bubble object. In the next step, the labels of each voxel are sorted by size and only the largest label defines the bubble diameter (Figure 5C). In the next step, the diameter of each voxel gets read out and the mean value is calculated, resulting in the mean size of the particle (Figure 5D). For a better estimation of grain diameter and structure, the mean value is selected here as grains are potentially asymmetric. Using IPL, it is possible to project the results of the global 3D analysis along the Z-axis (depth) for each slice enabling visualisation and quantification of features along the sample.

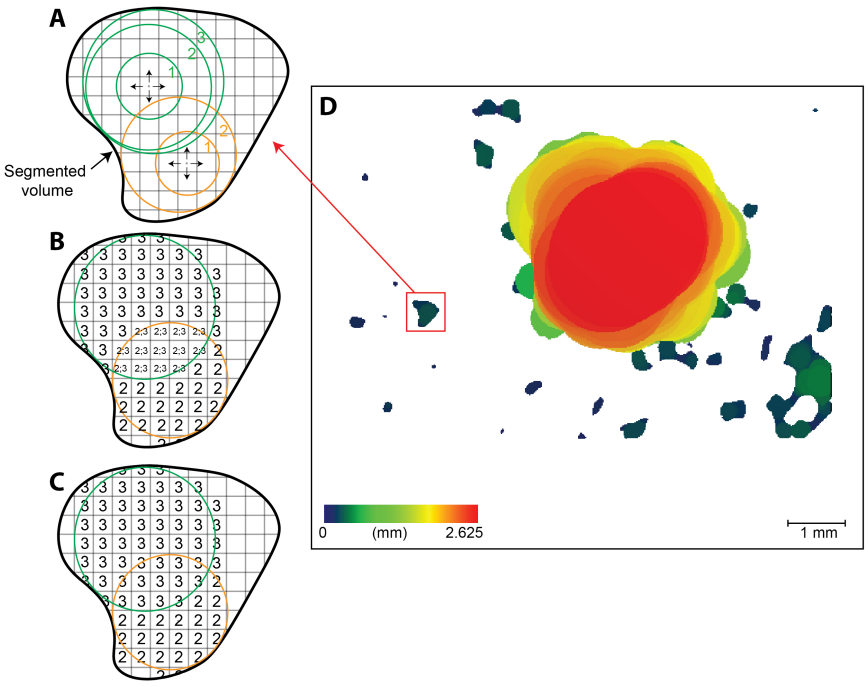

FIGURE 5 Detailed steps of the bubble growing algorithm used to compute particle sizes from micro-CT data. (A) Bubbles grow from randomly selected voxels and integrate neighbouring voxels until it hits two edges of the object (= potential short axis). (B) Each voxel belonging to the bubble is labelled by the potential short axis. This step is repeated until all voxels inside the analysed object are labelled by at least one bubble object. (C) For voxel with several labels, the largest is selected. The particle size is calculated from the mean value of each voxel. (D) Result of a slicewise extraction for the diameter of a particle. Colour code represents the highest value of each voxel contributing to the final measured diameter of a particle.

2.5 | Micro-XRF

Non-destructive micro-XRF analyses were carried out using a Bruker M4 Tornado at the Institute of Mineralogy and Petrography of the University of Innsbruck. The Bruker M4 Tornado uses a single rhodium target X-ray tube with up to 50 kV and 600 μA power and is equipped with a Be window. It focusses the beam with polycapillary optics down to a spot size of *ca* 25 μm. However, because of the large sample size and limited computer memory, the spot-size was fixed at 50 μm for the Gosau and Hecho samples and 70 μm for the Annot sample. This microanalytical instrument provides element mapping of the entire sample via the x-y moving stage. Maps of chemical element distribution are visualised using the function of "area analysis mapping" of the Brucker M4 Tornado software. By layering chemical elements together it is possible to interpret mineral phases and mineral distribution in the sample. This was later confirmed by mineral identification in thin section.

2.6 | Thin section

Thin sections cut on the surface plane where micro-XRF was measured have a standard thickness of 30 μm and were soaked in an epoxy resin. The Gosau turbidite sample could be accommodated on a single thin section, however, the Hecho and Annot samples were too long and each were made into two thin sections. The main mineral phases, matrix composition and cement type were characterised using a standard petrographic microscope.

2.7 | Grain-size analysis by thin section image analysis

Images of thin sections were acquired using the Zeiss Axio Imager A1m microscope and high-resolution IMAGINGSOURCE DFK33UX264 camera providing a resolution of 3616 dpi, and thus a resolution of *ca* 7 μm. Pictures were acquired automatically using the Petrog 5.0.3.5 software (PETROG System, Conwy Valley System Ltd, U.K.) along with a moving stage. To avoid problems during photograph stitching, a 10% overlap was chosen between each picture. Pictures were stitched together using Fiji (*Fiji Is Just ImageJ*; version 1.53q) software (Schindelin et al., 2012). Image processing procedures were implemented using Fiji and Matlab to separate the grains from the matrix (segmentation) and to evaluate the two-dimensional (2D) grain distribution throughout the sample, respectively. Details of thin section image processing are given in Supplemental Material S4. To be consistent with the evaluation of particle size computed from micro-CT data, the grain size computed from image analysis in thin section is based on the short-axis of a grain.

Before any processing, sample images were cropped to avoid artefacts from the background image of the thin section. For the preprocessing step, each stitched image of a thin section was converted to a greyscale (8-bit image). Noise was reduced by enhancing contrast (images are enhanced when the command *Equalize histogram* is checked) and by applying filters such as "Median" that replaces each pixel with the neighbourhood median.

For the segmentation step, different thresholds were later applied to produce a binary image. For each thin section image, two binary images were produced. A first image to which the darkest grains were isolated (e.g., clay or some feldspar) by choosing a range of relatively low grey-level values that were manually selected using the threshold sliders. A second binary image was produced where the lightest grains (e.g., quartz, carbonate and feldspar) were isolated by selecting a range of relatively high grey-level values with the threshold sliders. Attempts were made to visually cover the maximum number of grains and avoid the matrix for each range of threshold. Threshold values are different for each sample because of different mineral composition and settings during image acquisition (e.g., brightness) and thus different grey-level values. Using the plugin MorpholibJ in ImageJ, a distance transform watershed map (Distances: Quasi-Euclidean (1,1.41); output Type: 32 bits; Dynamic: 2.00; Connectivity: 4) was created, to separate the touching grains in the best possible way. Grain discretisation was improved by multiplying the original binary image by the distance transform watershed map. The resulting map was labelled using the MorpholibJ plugin ("*Set label map*"), so that each pixel corresponds to the integer index of the particle it belongs to. From the resulting map, the value of the short-axis of each grain along with its coordinates were exported using the MorpholibJ plugin in ImageJ. The grain-size data measured with ImageJ was analysed using the Matlab *grainmap* code from Falvard and Paris (2017) giving a grain-size map of the sample. Because values differed from those in the original Matlab code, the grain size (ranging from very-fine to coarse sand in this study) and colour bar scale were modified to best fit the dataset. This permits a 2D visualisation of the size and distribution of grains and structures along the sample.

3 | TERMINOLOGY

Sedimentary texture and structures—Sedimentary texture refers to the small-scale character of a rock such as the

shape, size, sorting and 3D arrangement of the component grains. Variations in textural characteristics are the product of physical (sediment transport), chemical (e.g., chemical reactions between particles and/or pore fluids) and biological processes (animal or plant life modifying sediments) (Collinson, 2019 and references therein). Only primary physical sedimentary structures were considered in this study. If physical conditions or sediment supply vary during transport, laminations of different character are often the result (Campbell, 1967), and it is these compositional and textural differences that make the sedimentary structure visible to the naked eye. Examples of common primary sedimentary structures in deep-marine sandstones are graded bedding, plane-parallel and cross lamination.

Grains versus particles—"Grains" are referred to here as the coarsest components of sandstones (> clay size). This includes detrital grains such as quartz, feldspar, calcite or dolomite. "Particles" are seen as volumes formed by homogeneous CT density distribution. The term "particle" is only used in the analysis of CT data. Grains with touching borders, a size below the CT- object resolution (< very-fine sand) and showing a homogeneous density distribution are seen as a single interconnected particle. In this case, and especially for the matrix component, the measured particle size is coarser than the true grain size.

Matrix—The fine-grained component (< very fine sand) filling the spaces between the detrital grains is referred to the matrix. Matrix is commonly composed of clay-sized and silt-sized calcite, dolomite, quartz or feldspar. In this paper, the cement is considered "matrix", as it cannot be distinguished with micro-CT techniques.

4 | RESULTS

4.1 | Upper-Cretaceous Gosau sample

4.1.1 | Observed micro-CT characteristics

The micro-CT image of the sample from the Gosau Formation (Figure 6A) shows a progressive decrease in the distribution of low-density particles (dark particles) from the base to the top of the sample (Figure 6B). The first centimetre at the base, composed mainly of low-density particles, shows no particular organisation. The remainder of the sample is composed mostly of alternating low-density and high-density particles forming millimetre-scale laminae (up to 5 mm thick) throughout the sample. The micro-CT image clearly shows a decrease in laminae thickness from the base to the top of the sample.

4.1.2 | Computed size and distribution of particles

Three density thresholds are defined (Figure 6C through F; Supplemental Material S3). The highest-density window ranges from 1605 to 2378 mgHA/cm^3. It shows a volume fraction of 0.025 and a mean particle size of 0.4725 mm (Table 1). High-density particles partially highlight the sedimentary structures; however, it is in a minor proportion. High-density particles fill most of the fracture that cross-cuts the sample (Figure 6D)—the significant increase in high-density particle size in the lower and middle part of Figure 6C is related to the presence of the fracture fill. Large computed particle size is due to limitations of the algorithm to calculate particle dimension lower than very-fine sand (see Section 5.4).

The middle-density window, ranging from 1189 to 1604 mgHA/cm^3, has a mean particle size of 0.3221 mm and a volume fraction of 0.7489 (Table 1). Middle-density particles are most likely related to the matrix (Figure 6E). In some cases where the matrix is composed mostly of silt-size particles below the resolvable object resolution of *ca* 63 µm (see Section5.4) and with the same CT density, the algorithm cannot identify particle edges (interconnected particles) and computes a coarse particle size. This is mainly confined to the sample edges (Figure 6E). This is considered an artefact and should not be considered in the analysis of particle distribution. It also results in a relatively large particle size as observed in Figure 6C.

The low-density window, ranging from 423 to 1188 mgHA/cm^3, shows a volume fraction of 0.1796 with a mean particle size of 0.136 mm (Table 1). Low-density particles demarcate the plane-parallel lamination (indicated by arrows in Figure 6F) with a decreasing laminae thickness and particle size towards the top of the sample. Sedimentary structures are visualised by the variation in particle size and volume fraction of the low-density particles as observed in Figure 6C.

4.1.3 | Micro-XRF

Two chemical-element assemblages are observed. The first one, marking out the lamination throughout the sample (light pink and yellow lamination in Figure 6G), consists of silica (pink) and potassium (yellow in Figure 6G). By combining these chemical elements, these laminations are likely composed of quartz (pink), K-feldspar (yellow) and clay (orange interpreted from the combination of silica (pink) and magnesium (brown) or silica and potassium (yellow)). In contrast, thicker laminae show a high content of magnesium, silica and calcium and are interpreted to be composed mainly of

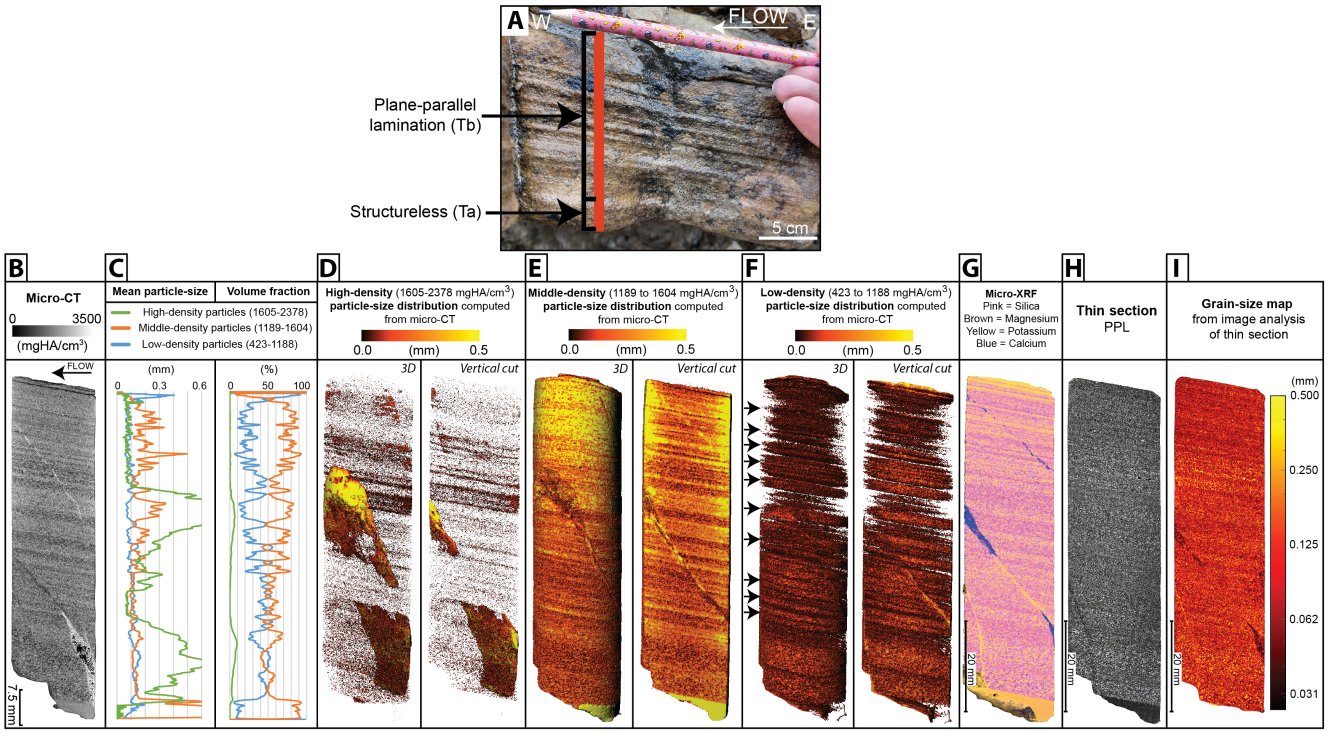

FIGURE 6 (A) Turbidite sampled from the Upper Cretaceous Gosau Group showing a structureless base overlain by plane-parallel lamination, that could be visually interpreted as T_a and T_b divisions of the Bouma sequence (Bouma, 1962), respectively. (B) Native micro-CT image. (C) Graphs showing computed particle size and volume fraction for each CT density window. Note that, in some places the mean size of high-density particles is >0.6 mm and coincides with the homogeneous density of the fracture fill crossing the sample, which is computed as large interconnected particles. (D) 3D distribution of high-density computed particle size and in a vertical cut oriented parallel to palaeoflow direction. (E) 3D distribution of middle-density computed particle size and in a vertical cut oriented parallel to the palaeoflow direction. (F) 3D distribution of low-density computed particle size and in a vertical cut oriented parallel to the palaeoflow direction. Arrows indicate parallel laminations. (G) Micro-XRF map. (H) Thin section image (PPL = plane-polarised light). (I) Grain-size map computed from thin section image analysis.

dolomite (brown) and clay (orange), which is most likely related to the matrix composition. This is confirmed by other chemical elements in Supplemental Material S5 and thin section analysis.

Combining the micro-CT and micro-XRF data suggests that the low-density particles correspond to the silicate fraction (e.g., quartz and feldspar) whereas the middle-density particles are related to the mixture of silicate and carbonate fractions that mainly form the matrix. The high-density particles correspond to the carbonate fraction and especially to calcite as shown by the fracture fill.

4.1.4 | Petrography and grain size

The Gosau sample is a poorly sorted arenite dominated by quartz with significant alkali feldspar (Figure 7). Micas and plagioclase are common and carbonate minerals are rare. Clay flocs are common and increase in abundance upward. Grains are sub-angular to sub-rounded. A fine-grained micritic carbonate matrix fills the space between larger detrital grains and some quartz and feldspar grains are surrounded by a calcite cement (Figure 7).

Grain-size analysis by image analysis of thin sections gives a grain size up to 0.50 mm (grain short axis). Mean grain size calculated for the light-coloured grain fraction is 0.0450 mm. Mean grain size computed for the dark-coloured grain fraction is 0.0476 mm (Table 1). A general fining upward trend is observed whereas individual laminae are demarcated by distinct and sharp changes in grain size (Figure 6I).

4.2 | Middle-Eocene Hecho sample

4.2.1 | Observed micro-CT characteristics

Micro-CT data of the Hecho sample (Figure 8A) shows a general mixture of high-density and low-density particles, although a progressive upward decrease in the proportion of high-density particles is noted (Figure 8B). No

TABLE 1 Summary table highlighting the detailed results of micro-CT, computed particle size from micro-CT for each density window, micro-XRF, optical petrography and computed grain size from thin section analysis for each sample.

	Gosau Group Sample, Poorly sorted arenite	**Hecho Group sample, Well to poorly sorted arenite**	**Annot Formation sample, Moderately well sorted arenite**
Naked-eye observed sedimentary structures	Structureless and plane-parallel lamination	None/Structureless	Plane-parallel, convolute and ripple-cross lamination
Observed micro-CT characteristics	Decrease in low-density particles from base to top Internal structures highlighted by low-density particles	Decrease in high-density particles from base to top Internal structures highlighted by low-density particles	Dominated by low-density particles Internal structures highlighted by high-density particles
Density thresholds (mgHA/cm^3)			
High density (HD)	1605–2378 (Bulk)	1453–2378 (Bulk)	1381–2378 (Internal structures)
Middle density (MD)	1189–1604 (Bulk)	1151–1452 (Bulk)	1071–1380 (Bulk)
Low density (LD)	423–1188 (Internal structures)	432–1150 (Internal structures)	423–1070 (Bulk)
Computed particle-size from micro-CT	**HD:** Mean particle size = 0.4725 mm Volume fraction = 0.025 *Fracture infill* **MD:** Mean particle size = 0.3221 mm Volume fraction = 0.7489 *No trend (matrix)* **LD:** Mean particle size = 0.136 mm Volume fraction = 0.1796 *Lamination*	**HD:** Mean particle size = 0.1392 mm Volume fraction = 0.2194 *Fining upward* **MD:** Mean particle size = 0.1928 mm Volume fraction = 0.7399 *No trend (matrix)* **LD:** Mean particle size = 0.1151 mm Volume fraction = 0.0399 *Lamination*	**HD:** Mean particle size = 0.0867 mm Volume fraction = 0.0186 *Lamination* **MD:** Mean particle size = 0.1281 mm Volume fraction = 0.5467 *No trend* **LD:** Mean particle size = 0.11 mm Volume fraction = 0.2738 *No trend*
Micro-XRF and chemical elements	Bulk (matrix) = Mg, Ca, Si Sedimentary structures = Si, K	Bulk (matrix) = Ca, Si, K, Mg	Bulk (matrix) = Si, K, Ca Sedimentary structures = K, Mg, Al
Petrography and computed grain-size from thin-section image analysis	Qz, Al-Feld dominant; micritic carbonate (dolomite) matrix, calcite cement Grain size up to 0.5 mm Mean light-grain size = 0.0450 mm Mean dark-grain size = 0.0476 mm	Qz, Feld, calcite dominant; micritic carbonate matrix, calcite cement Grain size up to 1 mm Mean light-grain size = 0.0491 mm Mean dark-grain size = 0.0490 mm	Qz, Feld, mica dominant; calcite minor; poor proportion of fine-grained matrix Grain size up to 0.75 mm Mean light-grain size = 0.0473 mm Mean dark-grain size = 0.0552 mm

internal sedimentary structure is observed. The patch of low-density particles in the middle of the sample is most likely related to bioturbation.

4.2.2 | Computed size and distribution of particles

Three density thresholds are identified (Figure 8C; Supplemental Material S3). The category of high-density particles ranges from 1453 to 2378 mgHA/cm^3 with a mean particle size of 0.1392 mm and a total volume fraction of 0.2194 (Table 1). Particle size observed in the high-density category shows a progressive upward decrease (Figure 8C), but no obvious internal structure is observed (Figure 8D).

The middle-density particles range from 1151 to 1452 mgHA/cm^3 with a mean particle size of 0.1928 mm and a volume fraction of 0.7399 (Table 1). The upward increase in particle size (Figure 8C,E) is related to the limits of the algorithm to compute particle size below very-fine sand (see Section 5.4). No internal structure is observed in this particle-size category (Figure 8E).

The low-density window ranges from 423 to 1150 mgHA/cm^3. It shows a mean particle size of 0.1151 mm and a total volume fraction of 0.0399 (Table 1). As observed in the graph of low-density particle size variation (Figure 8C) as well as in the 3D distribution of particles (Figure 8F), low-density particles show internal structures such as millimetre-thick plane-parallel lamination in the lower half of the sample and downflow-cross lamination in the upper half of the sample (as highlighted by arrows in Figure 8F).

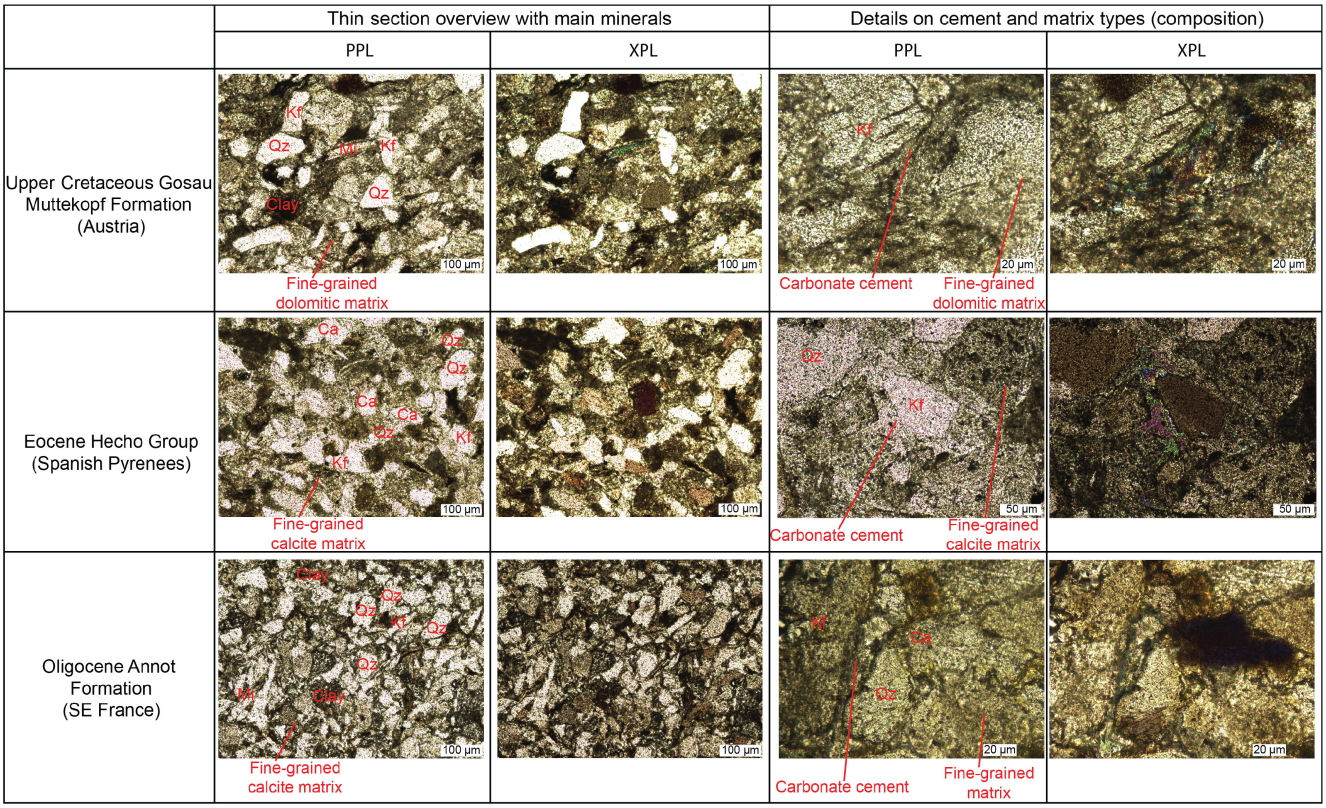

FIGURE 7 Chart of photomicrographs summarising the different mineral phases observed in thin sections from the three study areas. Qz = Quartz; Kf = Potassium feldspar; Mi = Mica; Ca = Calcite; PPL = plane-polarised light; XPL = Crossed-polarised light.

A progressive decrease in low-density particle size is observed from the base to the top of the sample (Figure 8C).

4.2.3 | Micro-XRF

The sample of the Eocene Hecho Group shows abundant calcium (attributed to calcite from thin section analysis) that decreases upward. Silica (=quartz) is also present throughout the sample (Figure 8G). No obvious internal sedimentary structure, as revealed by mineral segregation, is observed in the sample.

After alignment and comparison between micro-CT and micro-XRF data, it is inferred that calcite grains are related to the highest-density particles in the micro-CT. The middle-density particles representing the highest volume fraction, are related to the carbonate matrix. Finally, the lowest-density particles are related to the silicate fraction made up of quartz and feldspar grains.

4.2.4 | Petrography and grain size

The sandstone sample from the Eocene Hecho Group is classified as an arenite. Although, not a well-sorted arenite, the sorting is better than in the Gosau sample. The main mineral phases consist of quartz, feldspar (alkali feldspar and plagioclase) and carbonate minerals (e.g., calcite and dolomite) (Figure 7), the latter showing a decrease in abundance towards the top of the sample. Mica and clay flocks are abundant towards the top of the sample. Grains are subangular to sub-rounded. Like in the Gosau sample, a fine-grained micritic carbonate matrix fills the space between grains. Carbonate cement is common surrounding quartz and feldspar grains. Nummulites are also observed.

Based on thin section image analysis (Figure 8I), a progressive upward decrease in grain size is observed and the mean size of light-coloured (0.0491 mm) and dark-coloured (0.0490 mm) grains is virtually identical (Table 1).

4.3 | Oligocene Annot Formation sample

4.3.1 | Observed micro-CT characteristics

The micro-CT image of the Annot Formation sample (Figure 9A) shows the highest content of low-density particles throughout the sample (Figure 9C; Supplemental Material S3) compared to the Gosau and Hecho samples. The upper 2 cm of the sample, which represents the mud cap of the turbidite, consists mostly of middle-density particles.

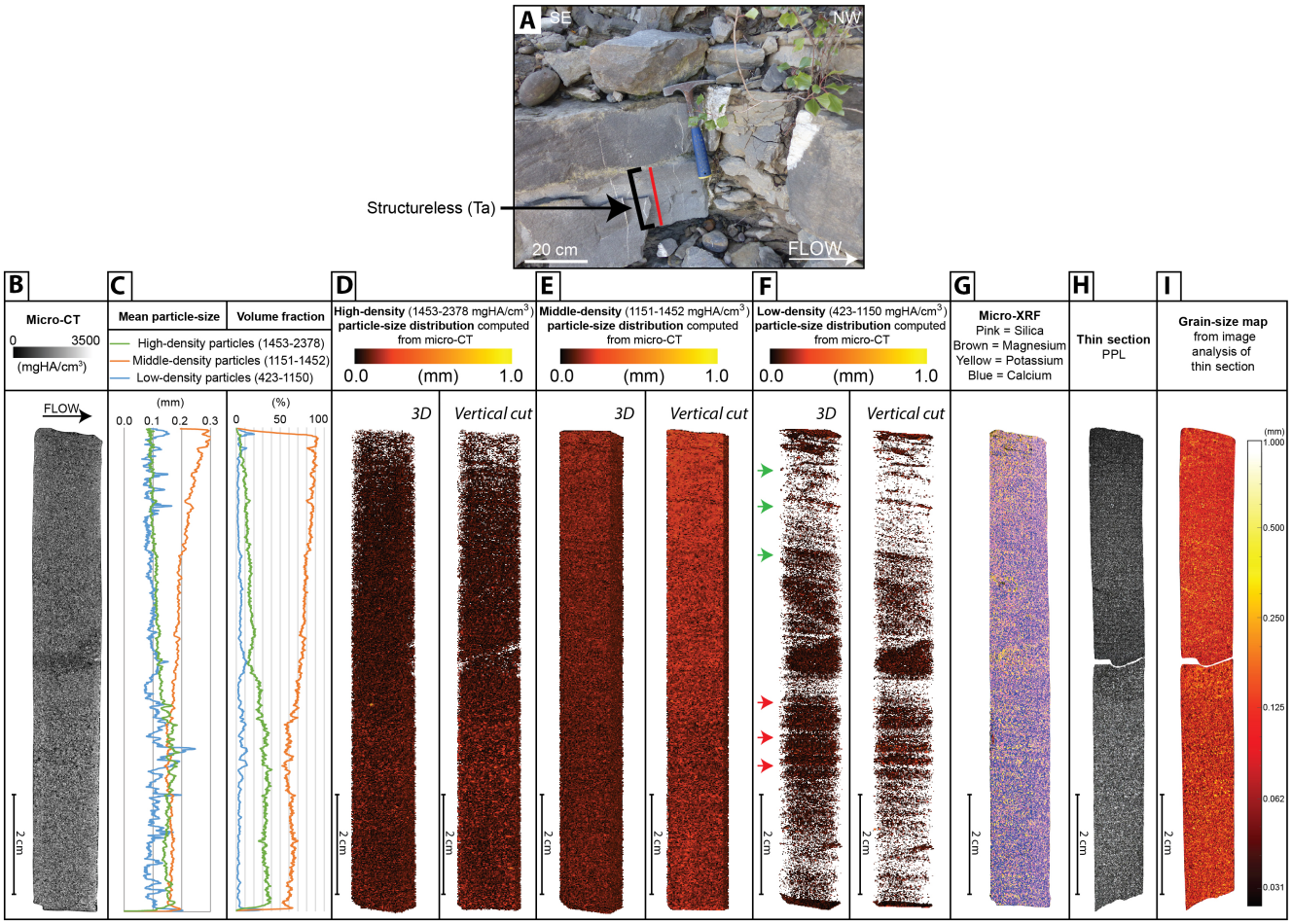

FIGURE 8 (A) Structureless turbidite from the Eocene Hecho Group, that could be visually interpreted as the T_a division of the Bouma sequence (Bouma, 1962). (B) Native micro-CT image. (C) Graphs showing computed particle size and volume fraction for each CT density window. (D) 3D distribution of high-density computed particle size and in a vertical cut oriented parallel to the palaeoflow direction. (E) 3D distribution of middle-density computed particle size and in a vertical cut oriented parallel to the palaeoflow direction. (F) 3D distribution of low-density computed particle size and in a vertical cut oriented parallel to the palaeoflow direction. Red arrows indicate plane-parallel lamination. Green arrows indicate downflow-cross lamination (G) Micro-XRF map. (H) Thin section image (PPL = plane-polarised light). (I) Grain-size map computed from thin section image analysis.

4.3.2 | Computed size and distribution of particles

The high-density particles range between 1381 to 2378 mgHA/cm^3 (Figure 9C). The high-density window shows the lowest volume fraction (0.0186) and the smallest mean particle size (0.0867 mm) (Table 1). The coarsest fraction of the high-density particles underlies the internal structures in the sample (Figure 9D), with mean particle size above 0.1 mm within the lamination at the base of the sample (Figure 9C). An increase in the mean particle size (>0.1 mm) is observed at the top of the sample, however, this is induced by the presence of clay (mud cap) and the limit of the algorithm computing particle size in this fine-grained material (see Section 5.4). Similar trends are exhibited by the middle-density and low-density particles.

The middle-density window (from 1071 to 1380 mgHA/cm^3) has the highest mean volume fraction in the sample (0.5467) and the largest mean particle size (0.1281 mm) (Table 1). Although they are not well resolved in the 3D reconstruction in Figure 9E, internal structures are characterised by a decrease or an increase in the volume fraction of the middle-density particles (Figure 9C). The middle density particle size progressively decreases upwards (Figure 9C). The marked decrease in the volume fraction at the top of the sample is related to the computing method as particles were analysed on a square rather than a delimited (with defined boundaries) sample due to time constraints (at least two additional days of computing). As for the high-density window, there is a significant increase in the mean particle size at the top of the sample (Figure 9E) due to the limits of the algorithm to compute very-fine particle size (see Section 5.4). Based on comparison with the micro-XRF

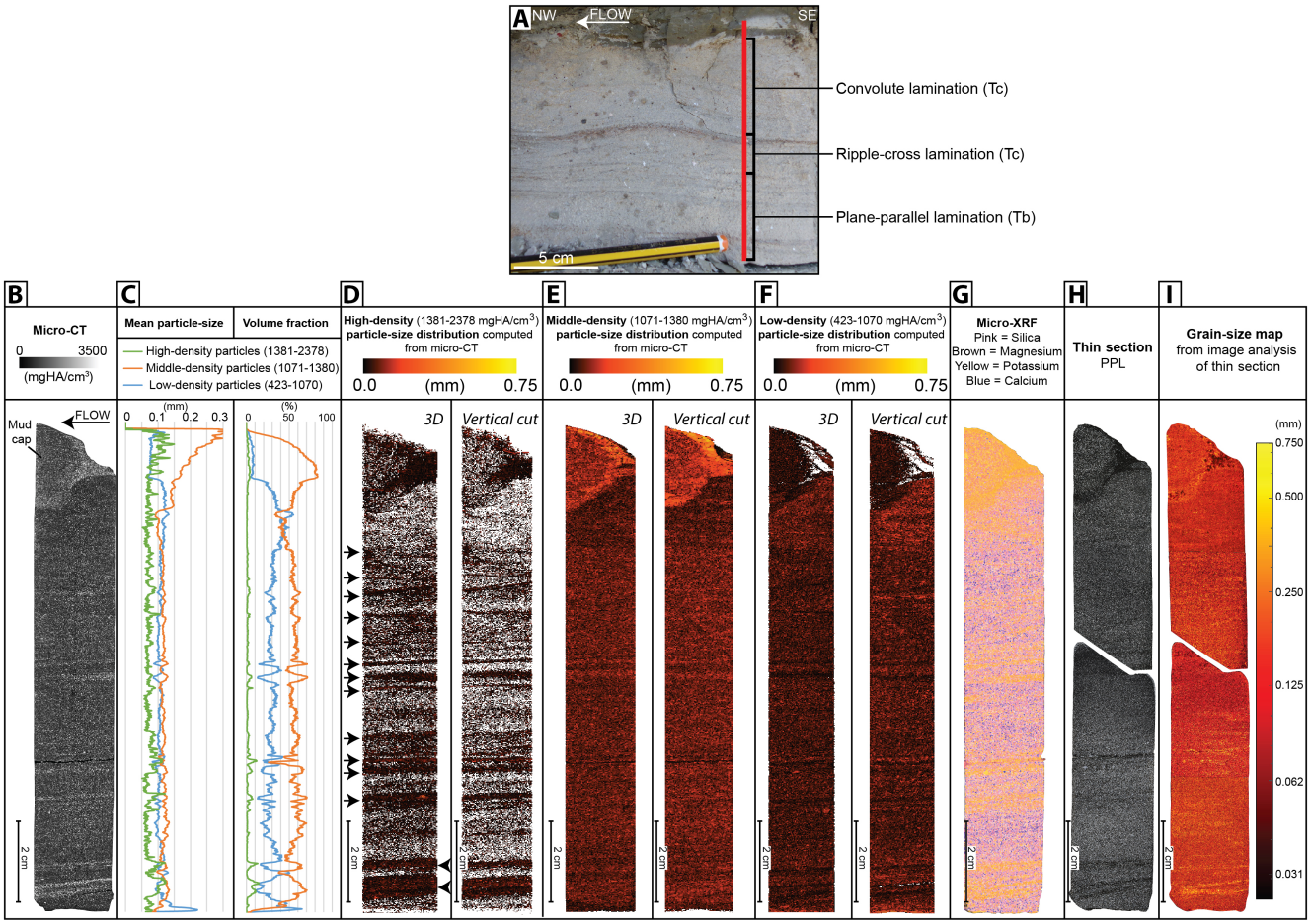

FIGURE 9 (A) Turbidite from the Annot Formation showing plane-parallel lamination overlain by ripple-cross and convolute lamination, that could be visually interpreted as the T_b and T_c divisions of the Bouma sequence (Bouma, 1962), respectively. (B) Native micro-CT image. (C) Graphs showing computed particle size and volume fraction for each CT density window. (D) 3D distribution of high-density computed particle size and in a vertical cut oriented parallel to the palaeoflow direction. Arrows indicate sedimentary structures. (E) 3D distribution of middle-density computed particle size and in a vertical cut oriented parallel to the palaeoflow direction. (F) 3D distribution of low-density computed particle size and in a vertical cut oriented parallel to the palaeoflow direction. (G) Micro-XRF map. (H) Thin section image (PPL = plane-polarised light). (I) Grain-size map computed from thin section image analysis.

map, it is inferred that the middle-density particles are most likely related to the fine-grained matrix.

The low-density window (from 423–1070 mgHA/cm^3) has a volume fraction of 0.2738 and a mean particle size of 0.11 mm (Table 1). As for the other density windows, variation in the volume fraction and particle size define laminations along the sample (Figure 9C). Similar to the middle-density window, the low-density window includes the fine-grained matrix.

4.3.3 | Micro-XRF

Compared to the Gosau and Hecho Group samples, the Annot sample is dominated by silica related to quartz (Figure 9G). Dark blue/ purple dots scattered throughout the sample (Figure 9G), are most likely due to the superposition of potassium, silica and calcium which can be attributed to feldspar (K-feldspar, plagioclase) minerals. Internal structures are highlighted by a high content of potassium and magnesium attributed to clay minerals (yellow/orange colour in Figure 9G). This is confirmed by the high aluminum content observed in the lamination (see Supplementary Material 5). Both quartz and feldspar are part of the bulk minerals of the sample, whereas laminations are formed by clay segregation. Calcium, and hence calcite was absent in the micro-XRF data.

Combined with the micro-XRF data, it is inferred that the high-density particles highlighting the lamination are most likely related to clay minerals. The low-density and middle-density particles, on the other hand, are related to the silicate fraction including quartz, feldspar and plagioclase.

4.3.4 | Petrography and grain size

The sandstone sample from the Oligocene Annot Formation is categorised as a moderately well-sorted arenite. Its composition can be characterised as a subarkose with the main detrital components being quartz, K-feldspar and mica (Figure 7). Calcite grains are also present and decrease upwards. Compared to the Gosau and Hecho formations there is a higher proportion of mica minerals and elongated clay minerals that highlight the internal sedimentary structures. A fine-grained matrix fills the space between the grains, however it is less abundant compared to the Gosau and Hecho samples. Calcite cement is present but rare (Figure 7).

Grain size calculated from thin section is up to 0.750 mm. The mean sizes for light-coloured and dark-coloured grains are 0.0473 mm and 0.0552 mm, respectively (Table 1). A progressive fining upward trend is observed. Some laminae are clearly visible in the computed grain-size map, such as coarse-grained lamination at the base of the sample (Figure 9I).

5 | DISCUSSION

5.1 | Micro-CT: a new tool to characterise textural properties and assess internal sedimentary structures

Sedimentary textures and structures resulting from fluid-particle interaction (Harms, 1979) are key in the interpretation of the physical conditions of SGF at the time of sediment deposition (Allen, 1982; Baas et al., 2004). Thus, it is necessary to assess internal sedimentary structures as accurately as possible to unravel flow characteristics. Internal sedimentary structures result from the segregation of grains due to differences in size, shape and density (Picha & Cline, 1973; Paola et al., 1989; Cheel, 1990; Best & Bridge, 1992; Collison, 2019). The latter corresponds to the mineralogical composition of the grains. As observed in the samples from this study, grain size and mineral composition are closely tied as the coarse-grained and fine-grained materials usually show different mineral composition. Although one of the limitations of most CT systems is the inability to discriminate between mineral types (overlap in X-ray attenuation), the X-ray attenuation is sufficiently different to distinguish between the silicate and carbonate fractions. In contrast, micro-CT techniques provide the opportunity to isolate grains based on their CT density values. This allows the isolation of the detrital grains commonly related to the coarsest fraction and highlighting sedimentary structures from the fine-grained matrix showing a different CT signature due to different mineral composition. Although it is valid and observed in all the studied samples, it is particularly well highlighted in the Gosau sample (Figure 6D,E,F).

The micro-CT technique is also useful for resolving sedimentary structures that are invisible to the naked eye, e.g. for samples that have a mineralogical and/or granulometric homogeneous appearance. For the Hecho sample, rich in carbonate grains and showing a carbonate-rich matrix, no sedimentary structures appear visible due to grain-size segregation. However, when isolating the detrital low-density silicate fraction, sedimentary structures appear to be visible on the micro-CT image (Figure 8F). A first approach of using CT techniques to study structureless deposits was already conducted by Hamblin (1965), where he detected "micro-cross lamination" in homogeneous sandstones. Although medical CT (Nelson et al., 2009) and micro-CT (Sabatier et al., 2022) are often used to highlight structures in homogeneous unconsolidated sediments, to the best of the authors knowledge, no micro-CT based study has been carried out to unravel the fabric of structureless lithified deposits. This study brings back into focus the interpretation of visually structureless deposits in the field (Allen, 1971; Hiscott & Middleton, 1980; Patel et al., 2022) stressing the need for analysing mineral composition and grain sorting of the deposits before reaching any interpretation in terms of depositional and/or post-depositional processes of structureless deposits. This example shows the significant potential of micro-CT to analyse sedimentary structures, especially when no sedimentary structures are macroscopically visible.

5.2 | Micro-CT versus thin section in the visualisation of internal sedimentary structures

There are many advantages in the use of micro-CT compared to thin section for resolving internal sedimentary structures: (i) the time commitment is comparatively short for micro-CT (about *ca* 15 min for coring the sample, *ca* 50 min per centimetre scanning, *ca* 2 hours of post processing, and *ca* 6 hours of computation) compared with thin section (several days for thin section production, and several hours for thin section analysis); (ii) micro-CT scanning is considered a non-destructive method in which structures of the sample are preserved whereas thin section production can be disruptive and even destructive (e.g., breaking the sample to fit the thin section size or impregnation preventing subsampling); (iii) the 3D volume and quantification of the sandstone component (based on their CT density phase) computed from micro-CT allows a better visualisation of structures (e.g., Hecho sample), something that is not possible in thin section

analysis; and (iv) it is possible to observe structures in every direction with micro-CT techniques whereas the plane of thin sectioning is rarely accurately aligned with the targeted structures which can lead to final misinterpretation, especially for complex 3D structures or changing structure orientation through the sample. Indeed, the micro-CT technique offers a better visualisation of the internal 3D structures of sandstones than the commonly used 2D characterisation tools such as thin sections with optical microscopy (Davis & Ethridge, 1975; Oren & Bakke, 2002; Asnussen et al., 2015; Bukharev et al., 2018), or higher magnification techniques like scanning electron microscopy (Krinsley et al., 1998; Bera et al., 2011), or simply with the naked eye in outcrop. Two dimensional images, especially 2D thin section images as presented in this study, do not provide the spatial relationship of sedimentary structures that can be much more complex in 3D (Figure 10). Direct comparison between thin section image and isolated 3D micro-CT density-window images show that sedimentary structures are better resolved in selected 3D density windows than in 2D (Figure 10). Micro-CT can give good indication on the lamination in 3D and thus on the palaeoflow direction or regime (e.g., orientation of cross-lamination), something that could be missed in 2D depending on the 2D view plane. Thus, 2D visualisation of sedimentary structures from thin section or by direct observation in outcrop can lead to a limited interpretation of the depositional processes at the origin of the structure.

From the evidence presented it is clear that 3D imaging by micro-CT techniques has considerable potential within the research of deep-marine sandstones. However, like any technique, it also has limitations (see Section 5.4 for details) and thin sections still provide information that cannot be obtained through micro-CT. Thin sections give an incomparable resolution of the physical properties within the sedimentary structures, enabling detailed fabric analysis at the grain scale, especially in case of grains finer than very fine sand. It is important to acknowledge that Bendle et al. (2015) observed comparable textural variation between micro-CT images of thin sections (*ca* 21.1 μm voxel size) and thin section images of glaciolacustrine unconsolidated sediments. However, they stipulated that there is a need to reduce the sample size (from 48,000 to 1000 mm^3) to generate such small voxel resolution and reach similar observation between micro-CT and thin section analysis.

As a consequence, depending on the research target, micro-CT does not represent a stand-alone replacement for thin section analysis in sandstones. Instead, micro-CT should be seen as a reliable companion method, with advantages like being time-saving, non-destructive, and allowing systematic visualisation of 3D sedimentary structures. If more details are needed about the grain fabrics

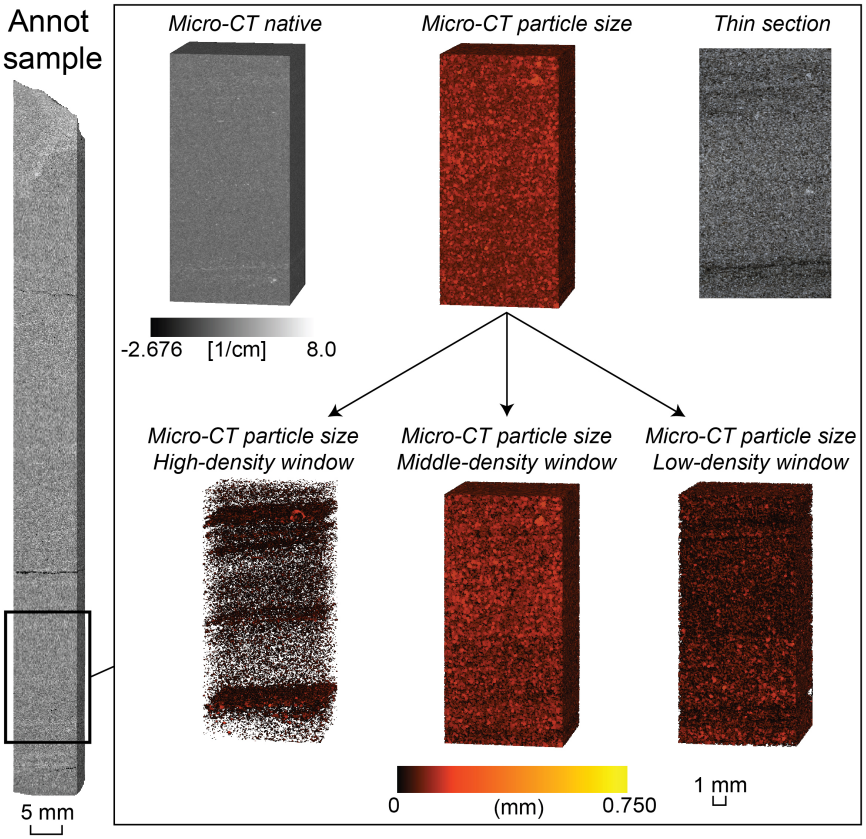

FIGURE 10 Comparison between the 3D micro-CT data and thin section image based on selected data near the base of the Annot sample. Isolation of the different density windows permits a better visualisation of the internal sedimentary structures, compared to the 2D thin section image.

or mineral composition forming the internal structures, micro-CT analysis should be complemented with (i) geochemical (e.g., XRF) or mineralogical analyses (e.g., X-ray diffraction) to correlate density windows to mineral phase and have a 3D rendered volume of each sandstone component and/or (ii) high-resolution petrographic analysis to obtain textural details at the grain scale.

5.3 | Micro-CT: towards a new tool to evaluate grain-size trends

Grain size reflects the energy level of SGFs and is related to the type of SGFs, while sorting is related mostly to the longitudinal grading of the SGFs (Walker, 1967; Komar, 1989; Hiscott, 1994; Dorrell et al., 2013). Thus, accurate and consistent measure of grain-size distribution in deep-marine sandstones are needed to better understand the processes at its origin. However, the determination of grain-size distribution in sandstones is problematic. The common sieving technique to measure the grain-size distribution in unconsolidated sediment does not apply efficiently to sandstones. Indeed, after disaggregation of cemented sandstones, the presence of broken grains or grain aggregates will bias the results. Until now, grain-size analysis of sandstones is typically based on point counting techniques in thin section (Ingersoll et al., 1984; Stevenson et al., 2020) or by image analysis of thin sections (Schäfer & Teyssen, 1987; Francus, 1998; Hüneke et al., 2021). Although the use of thin section analysis to measure grain size is valuable, there is still an on-going debate about the measurement of random sections through grains (apparent size) rather than their actual dimensions (true size) (Johnson, 1994; Buscombe, 2013), leading to a lack of consistency in the analysis of grain-size distribution (Figure 11).

In Earth Science, measuring grain size based on CT data is not new and has already been tested on ore deposits (Evans et al., 2015), individual targeted grains (e.g.,

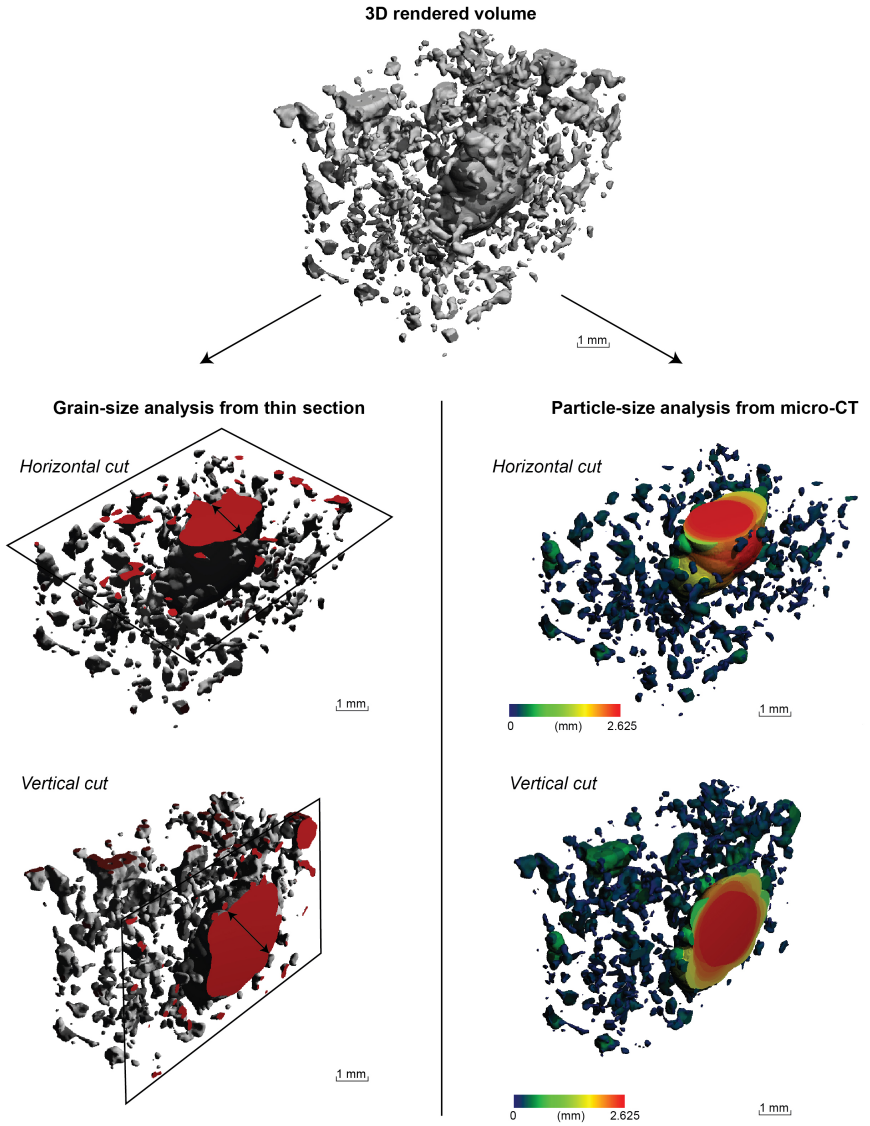

FIGURE 11 Illustration of the differences between grain size computed from thin section (left column) and particle size computed from micro-CT data (right column). Depending on the plane of observation in the thin section (here horizontal and vertical) the length of the grain short axis varies. In contrast, particle size computed from micro-CT data is similar irrespective of orientation and therefore provides more consistent particle-size data. Example from the Hecho Group turbidite.

apatite; Cooperdock et al., 2019) or on sediment-core samples (Orru et al., 2012; Paris et al., 2020; Al-Mufti et al., 2022). However, until now, the measurement of grain size from micro-CT data in sandstones has not been presented. Here the bubble growing algorithm of Hildebrand and Rüegsegger (1997) makes particle-size measurement from micro-CT sandstone data possible. One advantage of this technique compared to grain-size measurement from thin section, is the consistency of the results. Indeed, from micro-CT data, the same axis (short axis in this study) for each particle is measured thanks to its visualisation in 3D (Figure 11). The consistent particle-size measurement and the 3D visualisation provided by the micro-CT will lead to more reliable models of particle size and its trends, and thus to more accurate interpretations.

If we compare the grain-size maps obtained by image analysis of thin sections and the particle-size images computed from micro-CT data, grains and particles show comparable distributions along the three samples (see Figures 6I, 8I and 9I for grain-size map of each sample). This supports the use of micro-CT techniques to reconstruct size and distribution of grains. However, if the mean grain sizes obtained by thin section image analyses are compared to the mean particle sizes computed by micro-CT, some differences are noted. Indeed, mean grain size is one tenth smaller in thin section compared to computed mean particle size in micro-CT (Table 1). This is certainly related to the combination of: (1) limitation of the micro-CT algorithm to compute particle size smaller than very fine sand, which result in clusters of particles that are larger than the actual dimension of the component grains; and (2) selection of very small particles that are part of the matrix/cement (difficulty in differentiating very fine grains from matrix/cement) during image segmentation of thin section images.

5.4 | Limitations of the described algorithm and micro-CT

The maximum theoretical resolution of the micro-CT setup used in this study is 10.5 µm with a FOV of 21 mm. However, to improve the image quality, and thus the segmentation results, hardware binning was implemented, leading to an increased voxel size of 21 µm. This impacts directly on the resolvable grain size (> 63 µm) leading to the fact that (i) grains near the limit of resolution tend to be overestimated (as the potential partial volume effect leads to an increase in the particle volume) and (ii) grains below the resolution limit will be considered as an interconnected particle (as they cannot be separated from each other due to the partial volume effect). This is well illustrated in the three samples of this study, where the fine-grained matrix shows the largest mean particle size (see also discussion in Elkhoury et al., 2019). A solution to minimise the partial volume effect and increase the grain resolution would be to increase the scanning resolution. Another solution is to supersample images to artificially decrease the voxel size above the normally achievable resolution. Both of these solutions require an increase in exposure time per projection to keep the SNR on high levels (Peyrin et al., 1998).

Until now, another limitation of the algorithm used here is that no individual grain can be distinguished because of the inability to detect the boundaries between touching grains of the same CT density. Note that this does not affect the measured short-axis of the particle size computed by the algorithm. In the future, potential solutions to distinguish individual grains would be to implement and test 3D watershed methods (Higgins et al., 1993).

Due to the usage of a conventional X-ray source, only a trend in mineral composition (e.g., silicate versus carbonate fraction) can be observed in the micro-CT images. The potential of using synchrotron X-ray radiation may lead to higher contrast between mineral phases. Although synchrotron micro-CT has its potential, availability and costs are inhibiting factors. Another method to distinguish mineral phases could be the application of a dual energy CT. Dual energy settings make use of the fact that certain elements have different attenuation properties at different photon energies (Genant & Boyd, 1977). A problem with dual energy analysis is the 70 kV maximum voltage of the system. Indeed, low energies lead to penetration problems of the X-rays inducing significant cupping and streak artefacts (for high density minerals). As for dual energy CT a proper alignment is needed between the high and low energy scan, these artefacts make it nearly impossible to properly match the differences in attenuation to obtain the elemental information. Therefore, higher energy systems are required for dual energy evaluations.

Concerning the current subjective approach of CT density threshold selection, automated threshold estimation algorithms (e.g., OTSU thresholding; Otsu, 1979) were tested but no structural fitting solution was found. Current developments using artificial intelligence show promising results to provide a proper automated solution. However, the number of samples in this study is too small to provide a reliable training dataset.

5.5 | Wider implications for lithified sandstones

As shown by this study, the micro-CT technique is a new tool to better visualise the primary (depositional) fabric of sandstones providing a better assessment of internal

sedimentary structures (including the ones invisible to the naked eye) and a consistent appraisal of particle size distribution. Fabric development is directly linked to the palaeohydraulic conditions of the SGF during deposition (Middleton, 1965; Allen, 1970; Arnott & Hand, 1989; Baas, 2004; Sumner et al., 2008; Talling, 2013). Thus, micro-CT would be a valuable tool in reconstructing the physical flow conditions during deposition of deep-marine sandstone beds, including waning and waxing conditions. The opportunity to compute the volume of the coarse-grained fraction versus fine-grained (matrix) fraction could also give a more accurate interpretation on the type of deposits and related processes, for example, matrix-rich versus matrix-poor sandstones (Terlaky & Arnott, 2014; Ningthoujam et al., 2022).

The textural and mineralogical development of sandstone fabrics is almost equally universal in the sedimentary realm. Thus, the assessment of sandstone grain fabrics using micro-CT is not restricted to deep-marine sandstones but can also be applied to sandstones from a variety of depositional environments such as shallow-marine, fluvial and glaciogenic environments.

6 | CONCLUSIONS

This study explores the potential of micro-CT techniques to characterise textural properties and sedimentary structures in deep-marine sandstones. Because of the importance of the mineral composition in the formation, preservation and visualisation of sedimentary structures, micro-CT analysis is complemented with geochemical analysis based on micro-XRF mapping and petrographic analysis in thin sections. This multi-disciplinary approach is tested on three turbidite samples showing different mineral composition and textural properties: a poorly sorted arenite from the Gosau Group in the Muttekopf Basin (Austria); a well to poorly sorted arenite from the Hecho Group in the Ainsa Basin (Spain); and a moderately well sorted arenite from the Annot Formation (France).

Comparable distributions between particle size computed from micro-CT and grain size computed from thin section image analysis are documented, implying that micro-CT produces valuable data to reconstruct grain-size trends. The particle distribution permits a better visualisation of the texture, and thus sedimentary structures in 3D. By isolating particles based on their CT density, it is possible to separate the coarsest (detrital) fraction marking out the sedimentary structures from the fine-grained matrix. This technique allows the visualisation of sedimentary structures that otherwise are poorly resolved with the naked eye, especially in strata with uniform grain size and mineralogy.

Compared to 2D thin section analysis, there are many advantages in using micro-CT to analyse sediment textural properties. It is a non-destructive and time-saving technique as well as allowing a systematic visualisation of 3D sedimentary structures. Because of the limitations of micro-CT to identify mineral phases or to measure particles smaller than very fine sand, companion methods such as geochemical or high-resolution petrographic analyses are needed to provide supplemental information about grain fabric at the grain scale or mineral composition.

Micro-CT is an innovative tool to better visualise primary sedimentary structures in lithified SGF deposits, and thus an excellent technique to include in the reconstruction of palaeoflow conditions and depositional processes at the origin of the deposits.

ACKNOWLEDGEMENTS

Pauline Cornard is funded by the FWF Austrian Science Fund (Flow-Dynamic-Fan project M3065N). Simon Wagner is thanked for his help with micro-XRF analysis. Dominic Jaeger is thanked for his help in the acquisition of thin section images. We would like to thanks Pierre Francus, an anonymous reviewer and Editor Bill Arnott for their insightful suggestions that greatly improved the original manuscript.

DATA AVAILABILITY STATEMENT

The data that support the findings of this study are available from the corresponding author upon reasonable request.

ORCID

P. H. Cornard https://orcid.org/0000-0002-5034-937X
G. Degenhart https://orcid.org/0000-0002-9961-1084

REFERENCES

Al-Mufti, O.N., Arnott, R.W.C., Hinton, M.J., Alpay, S. & Russell, H.A. (2022) Using computed tomography (CT) to reconstruct depositional processes and products in the subaqueous glaciogenic Champlain Sea basin, Ottawa, Canada. *Geomorphology*, 403, 108165.

Allen, J.R.L. (1970) A quantitative model of grain size and sedimentary structures in lateral deposits. *Geological Journal*, 7(1), 129–146.

Allen, J.R.L. (1971) Massive beds in the central Pennine Basin: a discussion. *Proceedings of the Yorkshire Geological Society*, 38(2), 293–294.

Allen, J. (1982). *Sedimentary structures, their character and physical basis Volume 1*. New York: Elsevier, 593p.

Arnott, R.W.C. & Hand, B.M. (1989) Bedforms, primary structures and grain fabric in the presence of suspended sediment rain. *Journal of Sedimentary Research*, 59(6), 1062–1069.

Asmussen, P., Conrad, O., Günther, A., Kirsch, M. & Riller, U. (2015) Semi-automatic segmentation of petrographic thin section images using a "seeded-region growing algorithm" with an

application to characterize wheathered subarkose sandstone. *Computers & Geosciences*, 83, 89–99.

Baas, J.H. (2004) Conditions for formation of massive turbiditic sandstones by primary depositional processes. *Sedimentary Geology*, 166(3–4), 293–310.

Baas, J. H., Van Kesteren, W., and Postma, G. (2004). Deposits of depletive high-density turbidity currents: a flume analogue of bed geometry, structure and texture. *Sedimentology*, 51(5), 1053–1088.

Bam, L.C., Miller, J.A. & Becker, M. (2020) A mineral X-ray linear attenuation coefficient tool (MXLAC) to assess mineralogical differentiation for X-ray computed tomography scanning. *Minerals*, 10(5), 441.

Baraka-Lokmane, S., Main, I.G., Ngwenya, B.T. & Elphick, S.C. (2009) Application of complementary methods for more robust characterization of sandstone cores. *Marine and Petroleum Geology*, 26(1), 39–56.

Bendle, J.M., Palmer, A.P. & Carr, S.J. (2015) A comparison of micro-CT and thin section analysis of Late glacial glaciolacustrine varves from Glen Roy, Scotland. *Quaternary Science Reviews*, 114, 61–77.

Best, J.I.M. & Bridge, J. (1992) The morphology and dynamics of low amplitude bedwaves upon upper stage plane beds and the preservation of planar laminae. *Sedimentology*, 39(5), 737–752.

Bera, B., Mitra, S.K. & Vick, D. (2011) Understanding the micro structure of Berea Sandstone by the simultaneous use of micro-computed tomography (micro-CT) and focused ion beam-scanning electron microscopy (FIB-SEM). *Micron*, 42(5), 412–418.

Bertels, S.P., DiCarlo, D.A. & Blunt, M.J. (2001) Measurement of aperture distribution, capillary pressure, relative permeability, and in situ saturation in a rock fracture using computed tomography scanning. *Water Resources Research*, 37(3), 649–662.

Bouma, A.H. (1962) *Sedimentology of some flysch deposits. A graphic approach to facies interpretation*. Amsterdam: Elsevier, p. 168.

Boone, M., Dewanckele, J., Boone, M., Cnudde, V., Silversmit, G., Van Ranst, E. et al. (2011) Three-dimensional phase separation and identification in granite. *Geosphere*, 7(1), 79–86.

Bukharev, A.Y., Budennyy, S.A., Pachezhertsev, A.A., Belozerov, B.V. & Zhuk, E.A. (2018, September) Automatic analysis of petrographic thin section images of sandstone. In: *ECMOR XVI-16th European Conference on the Mathematics of Oil Recovery* (Vol. 2018, No. 1), pp. 1–10. Utrecht NL: European Association of Geoscientists & Engineers.

Buscombe, D. (2013) Transferable wavelet method for grain-size distribution from images of sediment surfaces and thin sections, and other natural granular patterns. *Sedimentology*, 60(7), 1709–1732.

Campbell, C.V. (1967) Lamina, laminaset, bed and bedset. *Sedimentology*, 8(1), 7–26.

Carlson, W.D. (2006) Three-dimensional imaging of earth and planetary materials. *Earth and Planetary Science Letters*, 249(3–4), 133–147.

Cartigny, M.J., Eggenhuisen, J.T., Hansen, E.W. & Postma, G. (2013) Concentration-dependent flow stratification in experimental high-density turbidity currents and their relevance to turbidite facies models. *Journal of Sedimentary Research*, 83(12), 1047–1065.

Cheel, R.J. (1990) Horizontal lamination and the sequence of bed phases and stratification under upper-flow-regime conditions. *Sedimentology*, 37(3), 517–529.

Cnudde, V., Boone, M., Dewanckele, J., Dierick, M., Van Hoorebeke, L. & Jacobs, P. (2011) 3D characterization of sandstone by means of X-ray computed tomography. *Geosphere*, 7(1), 54–61.

Cnudde, V. & Boone, M.N. (2013) High-resolution X-ray computed tomography in geosciences: A review of the current technology and applications. *Earth-Science Reviews*, 123, 1–17.

Coenen, J., Tchouparova, E. & Jing, X. (2004) Measurement parameters and resolution aspects of micro X-ray tomography for advanced core analysis. In Proceedings of International Symposium of the Society of Core Analysts.

Collinson, J. (2019) *Sedimentary structures*. Edinburgh SCT: Dunedin Academic Press Ltd.

Cooperdock, E.H., Ketcham, R.A. & Stockli, D.F. (2019) Resolving the effects of 2-D versus 3-D grain measurements on apatite (U–Th)/He age data and reproducibility. *Geochronology*, 1(1), 17–41.

Davies, D.K. & Ethridge, F.G. (1975) Sandstone composition and depositional environment. *AAPG Bulletin*, 59(2), 239–264.

Dorrell, R.M., Hogg, A.J. & Pritchard, D. (2013) Polydisperse suspensions: Erosion, deposition, and flow capacity. *Journal of Geophysical Research: Earth Surface*, 118(3), 1939–1955.

Elkhoury, J.E., Shankar, R. & Ramakrishnan, T.S. (2019) Resolution and limitations of X-ray micro-CT with applications to sandstones and limestones. *Transport in Porous Media*, 129(1), 413–425.

Evans, C.L., Wightman, E.M. & Yuan, X. (2015) Quantifying mineral grain size distributions for process modelling using X-ray micro-tomography. *Minerals Engineering*, 82, 78–83.

Falvard, S. & Paris, R. (2017) X-ray tomography of tsunami deposits: Towards a new depositional model of tsunami deposits. *Sedimentology*, 64(2), 453–477.

Feldkamp, L.A., Goldstein, S.A., Parfitt, M.A., Jesion, G. & Kleerekoper, M. (1989) The direct examination of three-dimensional bone architecture in vitro by computed tomography. *Journal of Bone and Mineral Research*, 4(1), 3–11.

Francus, P. (1998) An image-analysis technique to measure grain-size variation in thin sections of soft clastic sediments. *Sedimentary Geology*, 121(3–4), 289–298.

Genant, H.K. & Boyd, D. (1977) Quantitative bone mineral analysis using dual energy computed tomography. *Investigative Radiology*, 12(6), 545–551.

Ghorbani, Y., Becker, M., Petersen, J., Morar, S.H., Mainza, A. & Franzidis, J.P. (2011) Use of X-ray computed tomography to investigate crack distribution and mineral dissemination in sphalerite ore particles. *Minerals Engineering*, 24(12), 1249–1257.

Hamblin, W.K. (1965) *Internal structures of "homogeneous" sandstones*, Vol. 175. Kansas, US: Kansas Geological Survey Bulletin, 175, 569–582.

Harms, J.C. (1979) Primary sedimentary structures. *Annual Review of Earth and Planetary Sciences*, 7, 227–248.

Higgins, W.E. & Ojard, E.J. (1993) Interactive morphological watershed analysis for 3D medical images. *Computerized Medical Imaging and Graphics*, 17(4–5), 387–395.

Hildebrand, T. & Rüegsegger, P. (1997) A new method for the model-independent assessment of thickness in three-dimensional images. *Journal of Microscopy*, 185, 67–75.

Hiscott, R.N. (1994) Loss of capacity, not competence, as the fundamental process governing deposition from turbidity currents. *Journal of Sedimentary Research*, 64(2a), 209–214.

Hiscott, R.N. & Middleton, G.V. (1980) Fabric of coarse deep-water sandstones, Tourelle Formation, Quebec, Canada. *Journal of Sedimentary Research*, 50(3), 703–721.

Hüneke, H., Hernández-Molina, F.J., Rodríguez-Tovar, F.J., Llave, E. et al. (2021) Diagnostic criteria using microfacies for calcareous contourites, turbidites and pelagites in the Eocene–Miocene slope succession, southern Cyprus. *Sedimentology*, 68(2), 557–592.

Ingersoll, R.V., Bullard, T.F., Ford, R.L., Grimm, J.P., Pickle, J.D. & Sares, S.W. (1984) The effect of grain size on detrital modes: a test of the Gazzi-Dickinson point-counting method. *Journal of Sedimentary Research*, 54(1), 103–116.

Jerram, D.A., Mock, A., Davis, G.R., Field, M. & Brown, R.J. (2009) 3D crystal size distributions: A case study on quantifying olivine populations in kimberlites. *Lithos*, 112, 223–235.

Jiang, Z. (1995) The motion of sediment-water mixtures during intense bedload transport: computer simulations. *Sedimentology*, 42(6), 935–945.

Johnson, M.R. (1994) Thin section grain size analysis revisited. *Sedimentology*, 41(5), 985–999.

Ketcham, R.A. & Carlson, W.D. (2001) Acquisition, optimization and interpretation of X-ray computed tomographic imagery: applications to the geosciences. *Computers & Geosciences*, 27(4), 381–400.

Kim, K.Y., Zhuang, L., Yang, H., Kim, H. & Min, K.B. (2016) Strength anisotropy of Berea sandstone: results of X-ray computed tomography, compression tests, and discrete modeling. *Rock Mechanics and Rock Engineering*, 49(4), 1201–1210.

Kiminami, K. & Kontani, Y. (1979) Pre-Cretaceous paleocurrents of the northeastern Hidaka belt, Hokkaido, Japan. 北海道大学理学部紀要, 19(1–2), 179–188.

Komar, P.D. (1989) The hydraulic interpretation of turbidites from their grain sizes and sedimentary structures. *Sedimentology*, 32, 396–407.

Krinsley, D.H., Pye, K., Boggs, S., Jr. & Tovey, N.K. (1998) *Backscattered scanning electron microscopy and image analysis of sediments and sedimentary rocks*. New York, USA: Cambridge University Press.

Kuenen, P.H. (1966) Experimental turbidite lamination in a circular flume. *The Journal of Geology*, 74, 523–545.

Kumari, W.G.P., Ranjith, P.G., Perera, M.S.A., Li, X., Li, L.H. et al. (2018) Hydraulic fracturing under high temperature and pressure conditions with micro CT applications: geothermal energy from hot dry rocks. *Fuel*, 230, 138–154.

Kyle, J.R. & Ketcham, R.A. (2015) Application of high resolution X-ray computed tomography to mineral deposit origin, evaluation, and processing. *Ore Geology Reviews*, 65, 821–839.

Leclair, S.F. & Arnott, R.W.C. (2005) Parallel lamination formed by high-density turbidity currents. *Journal of Sedimentary Research*, 75(1), 1–5.

Legros, F. (2002) Can dispersive pressure cause inverse grading in grain flows? *Journal of Sedimentary Research*, 72(1), 166–170.

Lei, L., Seol, Y., Choi, J.H. & Kneafsey, T.J. (2019) Pore habit of methane hydrate and its evolution in sediment matrix–Laboratory visualization with phase-contrast micro-CT. *Marine and Petroleum Geology*, 104, 451–467.

McCoy, T.J., Ketcham, R.A., Wilson, L., Benedix, G.K., Wadhwa, M. & Davis, A.M. (2006) Formation of vesicles in asteroidal basaltic meteorites. *Earth and Planetary Science Letters*, 246((1–2)), 102–108.

Middleton, G.V. (1965) Primary sedimentary structures and their hydrodynamic interpretation. *SEPM Special Publication*, 12, 265.

Munkholm, L.J., Heck, R.J. & Deen, B. (2012) Soil pore characteristics assessed from X-ray micro-CT derived images and correlations to soil friability. *Geoderma*, 181, 22–29.

Mutti, E. (1977) Distinctive thin-bedded turbidite facies and related depositional environments in the Eocene Hecho Group (south-central Pyrenees, Spain). *Sedimentology*, 24, 107–131.

Nelson, H.M., Flemings, P.B., Germaine, J.T. & Dugan, B.E. (2009) Data report: radiography and X-ray CT imaging of whole core from IODP Expedition 308, Gulf of Mexico. In: Flemings, P.B., Behrmann, J.H., John, C.M. & the Expedition 308 Scientists (Eds.). Proc. IODP, 308: College Station, TX. (Integrated Ocean Drilling Program Management International, Inc.).

Ningthoujam, J., Wearmouth, C. & Arnott, R.W.C. (2022) Stratal characteristic and depositional origin of two-part (Mud-poor overlain by mud-rich) and associated deep-water strata: Components in a lateral depositional continuum related to particle settling in negligibly sheared mud-rich suspensions. *Journal of Sedimentary Research*, 92(6), 503–529.

Øren, P.E. & Bakke, S. (2002) Process based reconstruction of sandstones and prediction of transport properties. *Transport in Porous Media*, 46(2), 311–343.

Orru, C., Blom, A. & Uijttewaal, W. (2012) Laboratory measurements to determine the grain size distribution of a sand-gravel bed surface and substrate: image analysis and CT scanner analysis. In AGU Fall Meeting Abstracts (Vol. 2012, EP53B-1026).

Orsi, T.H., Edwards, C.M. & Anderson, A.L. (1994) X-ray computed tomography: a nondestructive method for quantitative analysis of sediment cores. *Journal of Sedimentary Research*, 64(3), 690–693.

Otani, J., Watanabe, Y. & Chevalier, B. (2010) Introduction of X-ray CT application in geotechnical engineering–theory and practice. In: *IOP Conference Series: Materials Science and Engineering (10,012089)*. Bristol, UK: IOP Publishing.

Otsu, N. (1979) A threshold selection method from gray-level histograms. *IEEE Transactions on Systems, Man, and Cybernetics*, 9(1), 62–66.

Ortner, H. (2001) Growing folds and sedimentation of the Gosau Group, Muttekopf, Northern Calcareous Alps, Austria. *International Journal of Earth Sciences*, 90(3), 727–739.

Ortner, H., Kositz, A., Willingshofer, E. & Sokoutis, D. (2016) Geometry of growth strata in a transpressive fold belt in field and analogue model: Gosau Group at Muttekopf, Northern Calcareous Alps, Austria. *Basin Research*, 28(6), 731–751.

Paola, C., Wiele, S.M. & Reinhart, M.A. (1989) Upper-regime parallel lamination as the result of turbulent sediment transport and low-amplitude bed forms. *Sedimentology*, 36, 47–59.

Paris, R., Falvard, S., Chagué, C., Goff, J., Etienne, S. & Doumalin, P. (2020) Sedimentary fabric characterized by X-ray tomography: A case-study from tsunami deposits on the Marquesas Islands, French Polynesia. *Sedimentology*, 67(3), 1207–1229.

Patel, U.S., Stow, D.A., Gardiner, A. & Buckman, J. (2022) Textual heterogeneity in massive sandstones from the Grès d'Annot and Numidian Flysch: Implications for depositional processes. *Journal of Sedimentary Research*, 92(4), 321–352.

Penkrot, M.L., Jaeger, J.M., Cowan, E.A., St-Onge, G. & LeVay, L. (2018) Multivariate modeling of glacimarine lithostratigraphy combining scanning XRF, multisensory core properties, and CT imagery: IODP Site U1419. *Geosphere*, 14, 1935–1960.

Peyrin, F., Salome, M., Cloetens, P., Laval-Jeantet, A.M., Ritman, E. & Rüegsegger, P. (1998) Micro-CT examinations of trabecular

bone samples at different resolutions: 14, 7 and 2 micron level. *Technology and Health Care*, 6(5–6), 391–401.

Picha, F. & Cline, L.M. (1973) Radiographic investigation of laminated and ripple cross-laminated flysch sandstones, Ouachita Mountains, Oklahoma. *Journal of Sedimentary Research*, 43(2), 466–470

Pickering, K.T. & Hilton, V.C. (1998) *Turbidite systems of south-east France: Application to hydrocarbon prospectivity*. Sutton Coldfield, UK: Vallis Press.

Polacci, M., Mancini, L. & Baker, D.R. (2010) The contribution of synchrotron X-ray computed microtomography to understanding volcanic processes. *Journal of Synchrotron Radiation*, 17, 215–221.

Rüegsegger, P., Koller, B. & Müller, R. (1996) A microtomographic system for the nondestructive evaluation of bone architecture. *Calcified Tissue International*, 58(1), 24–29.

Sabatier, P., Moernaut, J., Bertrand, S., Van Daele, M., Kremer, K., Chaumillon, E. & Arnaud, F. (2022) A review of event deposits in lake sediments. *Quaternary*, 5(3), 34.

Schäfer, A. & Teyssen, T. (1987) Size, shape and orientation of grains in sands and sandstones—image analysis applied to rock thin-sections. *Sedimentary Geology*, 52(3–4), 251–271.

Schindelin, J., Arganda-Carreras, I., Frise, E., Kaynig, V., Longair, M., Pietzsch, T., Preibisch, S., Rueden, C., Saalfeld, S., Schmid, B., Tinevez, J.Y., White, D.J., Hartenstein, V., Eliceiri, K., Tomancak, P. & Cardona, A. (2012) Fiji: an open-source platform for biological-image analysis. *Nature Methods*, 9(7), 676–682.

Schmitt, M., Halisch, M., Müller, C. & Fernandes, C.P. (2016) Classification and quantification of pore shapes in sandstone reservoir rocks with 3-D X-ray micro-computed tomography. *Solid Earth*, 7(1), 285–300.

Siddiqui, S., Funk, J.J. & Al-Tahini, A.M. (2010) Use of X-ray CT to measure pore volume compressibility of Shaybah carbonates. *SPE Reservoir Evaluation & Engineering*, 13(01), 155–164.

Singh, N., Kumar, S., Udawatta, R.P., Anderson, S.H., de Jonge, L.W. & Katuwal, S. (2021) X-ray micro-computed tomography characterized soil pore network as influenced by long-term application of manure and fertilizer. *Geoderma*, 385, 114872.

Sleutel, S., Cnudde, V., Masschaele, B., Vlassenbroek, J., Dierick, M., Van Hoorebeke, L. et al. (2008) Comparison of different nano- and micro-focus X-ray computed tomography set-ups for the visualization of the soil microstructure and soil organic matter. *Computers & Geosciences*, 34(8), 931–938.

Sok, R.M., Knackstedt, M.A., Varslot, T., Ghous, A., Latham, S. & Sheppard, A.P. (2010) Pore scale characterization of carbonates at multiple scales: Integration of Micro-CT, BSEM, and FIBSEM. *Petrophysics—The SPWLA Journal of Formation Evaluation and Reservoir Description*, 51(06), 379–387.

Su, Y., Zha, M., Jiang, L., Ding, X., Qu, J., Jin, J. & Iglauer, S. (2022) Pore structure and fluid distribution of tight sandstone by the combined use of SEM, MICP and X-ray micro-CT. *Journal of Petroleum Science and Engineering*, 208, 109241.

Stevenson, C.J., Peakall, J., Hodgson, D.M., Bell, D. & Privat, A. (2020) TB or not TB: banding in turbidite sandstones. *Journal of Sedimentary Research*, 90(8), 821–842.

Stow, D.A.V. & Piper, D.J.W. (1984) Deep-water fine-grained sediments: facies models. *Geological Society, London, Special Publications*, 15(1), 611–646.

Sumner, E.J., Amy, L.A. & Talling, P.J. (2008) Deposit structure and processes of sand deposition from decelerating sediment suspensions. *Journal of Sedimentary Research*, 78(8), 529–547.

Talling, P.J. (2013) Hybrid submarine flows comprising turbidity current and cohesive debris flow: Deposits, theoretical and experimental analyses, and generalized models. *Geosphere*, 9(3), 460–488.

Terlaky, V. & Arnott, R.W.C. (2014) Matrix-rich and associated matrix-poor sandstones: avulsion splays in slope and basin-floor strata. *Sedimentology*, 61(5), 1175–1197.

Tiwari, P., Deo, M., Lin, C.L. & Miller, J.D. (2013) Characterization of oil shale pore structure before and after pyrolysis by using X-ray micro CT. *Fuel*, 107, 547–554.

Van Daele, M., Cnudde, V., Boone, M., Deprez, M. & De Batist, M. (2016) On how X-ray (micro) computed tomography on turbidites can help us unravel paleoflow successions, directions and dynamics. In EGU General Assembly Conference Abstracts (pp. EPSC2016-12825).

Vermassen, F., Van Daele, M., Praet, N., Cnudde, V., Kissel, C. & Anselmetti, F.S. (2023) Unravelling megaturbidite deposition: Evidence for turbidite stacking/amalgamation and seiche influence during the 1601 ce earthquake at Lake Lucerne, Switzerland. *Sedimentology*, 70, 1496–1520.

Vergés, J., Fernàndez, M. & Martínez, A. (2002) The Pyrenean orogen: pre-, syn-, and post-collisional evolution. In: Rosenbaum, G. and Lister, G. S., 2002. Reconstruction of the evolution of the Alpine-Himalayan orogeny. *Journal of the Virtual Explorer*, 8, 57–76.

Walker, R.G. (1967) Turbidite sedimentary structures and their relationship to proximal and distal depositional environments. *Journal of Sedimentary Research*, 37(1), 25–43.

Wagreich, M. & Faupl, P. (1994) Palaeogeography and geodynamic evolution of the Gosau Group of the northern Calcareous Alps (Late Cretaceous, eastern Alps, Austria). *Palaeogeography, Palaeoclimatology, Palaeoecology*, 110(3–4), 235–254.

Wildenschild, D. & Sheppard, A.P. (2013) X-ray imaging and analysis techniques for quantifying pore-scale structure and processes in subsurface porous medium systems. *Advances in Water Resources*, 51, 217–246.

Wils, K., Deprez, M., Kissel, C., Vervoort, M., Van Daele, M., Daryono, M.R. et al. (2021) Earthquake doublet revealed by multiple pulses in lacustrine seismo-turbidites. *Geology*, 49(11), 1301–1306.

Yang, S.Q., Yang, Z., Jing, H.W. & Xu, T. (2020) Fracture evolution mechanism of hollow sandstone under conventional triaxial compression by X-ray micro-CT observations and three-dimensional numerical simulations. *International Journal of Solids and Structures*, 190, 156–180.

SUPPORTING INFORMATION

Additional supporting information can be found online in the Supporting Information section at the end of this article.

How to cite this article: Cornard, P.H., Degenhart, G., Tropper, P., Moernaut, J. & Strasser, M. (2023) Application of micro-CT to resolve textural properties and assess primary sedimentary structures of deep-marine sandstones. *The Depositional Record*, 00, 1–22. Available from: https://doi.org/10.1002/dep2.261